



Impacts of North American forest cover changes on the North Atlantic ocean circulation

Victoria M. Bauer¹, Sebastian Schemm¹, Raphael Portmann^{2,6}, Jingzhi Zhang¹, Gesa K. Eirund³, Steven J. De Hertog^{4,5}, and Jan Zibell¹

¹Institute for Atmospheric and Climate Science, ETH Zurich, Zurich, Switzerland.

²Agroscope Reckenholz, Climate and Agriculture, Division of Agroecology and Environment, Zurich, Switzerland

³Institute for Biogeochemistry and Pollutant Dynamics, ETH Zurich, Zurich, Switzerland

⁴Department of Water and Climate, Vrije Universiteit Brussel, Brussels, Belgium

⁵Q-ForestLab, Department of Environment, Universiteit Gent, Ghent, Belgium

⁶Present address: planval, Bern, Switzerland

Correspondence: Victoria M. Bauer (victoria.bauer@usys.ethz.ch)

Abstract. Atmosphere-ocean heat fluxes in the North Atlantic Labrador Sea region are a key driver of deep water formation and the Atlantic Meridional Overturning Circulation (AMOC). Previous research has shown that anthropogenic warming leads to reduced ocean heat loss and thereby reduced deep mixing in the North Atlantic. This results in AMOC decline and causes regional cooling of sea surface temperatures (SSTs) which has been referred to as the North Atlantic warming hole (NAWH).

5 Similar responses of the AMOC and the formation of a NAWH have been found for changes in wind stress and fresh water forcing in the North Atlantic. Moreover, recent research has also revealed such an AMOC and North Atlantic SST response in global-scale forestation experiments and a reversed response in deforestation experiments. Here, we test the hypothesis that forest cover changes in particular over North America are an important driver of this response in the downstream North Atlantic ocean. To this end, we perform simulations using the fully coupled Earth system model CESM2 where pre-industrial
10 vegetation-sustaining areas over North America are either completely forested (*forestNA*) or turned into grasslands (*grassNA*), and compare it to the control scenario without any forest cover changes. Our results show that North American forestation and deforestation induce a North Atlantic warming and cooling hole, respectively. Furthermore, the response is qualitatively similar to previously published results based on global extreme land cover change scenarios. Forest cover changes mainly impact the ocean through modulating land surface albedo and, subsequently, air temperatures. Around 80% of the ocean heat
15 loss in the Labrador Sea occurs within comparably short-lived cold air outbreaks (CAOs) during which the atmosphere is colder than the underlying ocean. A warmer atmosphere in *forestNA* compared to the control scenario results in fewer CAOs over the ocean and thereby reduced ocean heat loss, with the opposite being true for *grassNA*. The induced SST responses further decrease CAO frequency in *forestNA* and increase it in *grassNA*. Lagrangian backward trajectories starting from CAOs over the Labrador Sea confirm that their source regions include (de-)forested areas. A closer inspection of the ocean circulation
20 reveals that the subpolar gyre circulation is more sensitive to ocean density changes driven by heat fluxes than to changes in wind forcing modulated by land surface roughness. In *forestNA*, sea ice growth and the corresponding further reduction of ocean-to-atmosphere heat fluxes forms an additional positive feedback loop. Conversely, a buoyancy flux decomposition shows

<https://doi.org/10.5194/egusphere-2024-2087>

Preprint. Discussion started: 19 July 2024

© Author(s) 2024. CC BY 4.0 License.



that freshwater forcing only plays a minor role for the ocean density response in both scenarios. Overall, this study shows that forest cover changes over North America alter the frequency of CAOs over the North Atlantic and, as a consequence, the circulation of the North Atlantic. This highlights the relevance of CAOs for the formation of North Atlantic SST anomalies.

25



1 Introduction

Forests provide habitats for numerous species, offer valuable ecosystem services, and act as carbon sinks. The latter makes afforestation and reforestation (hereafter summarized under the term forestation) an attractive carbon mitigation strategy, alongside minimizing carbon emissions, to combat global temperature rise (Mo et al., 2023; Rohatyn et al., 2022; Bastin et al., 2019). In addition to absorbing carbon from the atmosphere, forestation locally promotes evapotranspiration and shading from direct shortwave radiation, decreases surface albedo, and increases surface roughness, while deforestation has the opposite effects (Bonan, 2008; Mahmood et al., 2014). The influence of these so-called biogeophysical effects extends beyond the local scale and can have significant impacts in remote areas (Portmann et al., 2022; Hua et al., 2023; Snyder, 2010; Swann et al., 2012). In particular, albedo changes following forestation contribute to warming at the global scale, while the albedo effect of deforestation contributes to a cooling (De Hertog et al., 2023; Portmann et al., 2022; Winckler et al., 2019; Jiao et al., 2017; Davin and de Noblet-Ducoudre, 2010; Snyder et al., 2004). Depending on the considered region, the albedo effect of large-scale forestation or deforestation can partly or fully offset the carbon effect (Weber et al., 2024; Jayakrishnan and Bala, 2023; Bonan, 2008; Bala et al., 2007; Renssen et al., 2003; Betts, 2000). The dominating effect depends heavily on latitude: While large-scale forestation in the tropics tends to have a net cooling effect (carbon and evapotranspiration effects dominating), boreal forestation leads to a net warming on the global scale (albedo effect dominating), and vice versa for deforestation (Rohatyn et al., 2022; Windisch et al., 2021; Li et al., 2015; Wang et al., 2014; Betts, 2000). Moreover, the response to extreme high latitude land cover changes was been shown to differ between continents in the past, with North America showing a comparably strong albedo response (Guo et al., 2024; Asselin et al., 2022).

Beyond the named biogeophysical effects, forestation has been found to also induce anomalies in the ocean. Yet, of the above studies, only some incorporated a dynamic ocean model response to forest cover changes (Guo et al., 2024; De Hertog et al., 2023; Hua et al., 2023; Portmann et al., 2022; Davin and de Noblet-Ducoudre, 2010; Wang et al., 2014; Winckler et al., 2019; Bala et al., 2007; Snyder et al., 2004; Renssen et al., 2003) and of those a limited number have thus far analyzed the ocean response (Guo et al., 2024; Jayakrishnan and Bala, 2023; Portmann et al., 2022; Davin and de Noblet-Ducoudre, 2010; Bala et al., 2007; Renssen et al., 2003). However, in several of these land use change experiments that adopted a dynamic ocean, the North Atlantic ocean featured a sea surface temperature (SST) anomaly of the opposite sign to the surrounding land and ocean, i.e. a local cooling in an otherwise warmer surrounding environment and vice versa (Guo et al., 2024; De Hertog et al., 2023; Boysen et al., 2020; Davin and de Noblet-Ducoudre, 2010; Bala et al., 2007). The emergence of such SST anomalies is herein referred to as a North Atlantic warming hole (NAWH) for a cool anomaly, as adopted in the literature addressing North Atlantic ocean variability (Keil et al., 2020; Gervais et al., 2018), and as a cooling hole (NACH) for the opposite phenomenon. A recent study (Portmann et al., 2022) investigated the climate response to global-scale forest cover changes focusing on the role of the global atmosphere and ocean circulation. Using the Community Earth System Model (CESM) version 2, the authors found a NAWH accompanied by a decrease in the Atlantic Meridional Overturning Circulation (AMOC) strength in response to global warming induced by large-scale forestation. Conversely, global deforestation resulted in a NACH and long-term increases in AMOC strength w.r.t. a control simulation. Another recent study (Guo et al., 2024) performed deforestation experiments



60 for each continent. Their North American and Eurasian vegetation removal experiments, conducted with CESM version 1, also showed a prominent cooling hole in the North Atlantic. Hereby, it is important to note that recent studies have found considerable model dependency of the climate response to vegetation changes (De Hertog et al., 2024, 2023). Nevertheless, the physical mechanisms responsible for these changes in ocean circulation and the formation of the SST anomalies in response to forest cover changes remain open.

65 The NAWH is also a prominent feature in future climate projections and in observations over the last century (Rahmstorf et al., 2015; Keil et al., 2020; He et al., 2022; Liu et al., 2020; Menary and Wood, 2018). Its emergence has been linked to changes in ocean circulation, in particular the AMOC (Gervais et al., 2018; Caesar et al., 2018; Rahmstorf et al., 2015). Specifically, studies have pointed towards a causal relationship between the concurrent cooling of North Atlantic SSTs and a potential slowing of the AMOC in response to global warming (van Westen et al., 2024; Ditlevsen and Ditlevsen, 2023; 70 Rahmstorf, 2002; Armstrong McKay et al., 2022; Keil et al., 2020). Research in the context of climate change, including the paleoclimate, has indicated that the ocean circulation may change drastically in response to atmospheric forcing with strong feedbacks on the terrestrial climate (Rahmstorf, 2002; Ditlevsen and Ditlevsen, 2023; van Westen et al., 2024). The cooling of the North Atlantic was shown to potentially cool large extents of the Arctic and Eurasia and lead to shifts in the climate system on the timescale of several centuries (Henry et al., 2016; Lynch-Stieglitz, 2017; Lenton et al., 2008; Gervais et al., 2019).

75 From an energy budget perspective, a sufficiently large hemispherically asymmetric perturbation influences both atmospheric and oceanic heat transport (e.g. Portmann et al., 2022). Our study, however, does not focus on arguing with zonal mean budget constraints but local-scale processes instead. Conceptually, in the subpolar North Atlantic, a warmer boreal atmosphere leads to reduced heat loss of the ocean to the atmosphere, which results in decreased deep water formation (DWF) and AMOC strength (Liu et al., 2020; Keil et al., 2020). The subsequent decrease in warm water import into the North Atlantic results in a cold 80 SST anomaly. Next to temperature, salinity is another main driver of deep water formation in the North Atlantic. For example, Liu et al. (2019) showed that the thermal and haline contributions to AMOC decline in response to Arctic sea ice decline were of similar magnitude. Specifically, increased buoyancy from enhanced freshwater influxes was comparable to the increase in buoyancy due to ocean warming, resulting from enhanced exposure to radiation. Conversely, Liu et al. (2020) found that manually reducing freshwater fluxes in anthropogenic warming simulations lead to a stabilization of the AMOC. Moreover, as 85 the second large-scale ocean circulation pattern in the North Atlantic, the subpolar gyre circulation also modulates the transport of salty waters and thus DWF and the NAWH (Keil et al., 2020; Fan et al., 2021; Böning et al., 2023; Gervais et al., 2018; Liu et al., 2019). Recently, underlying atmospheric drivers of DWF and the SST anomalies have received more attention: Changes in wind stress have been found to play an important role by modulating the subpolar gyre and subsequently DWF, resulting in positive and negative SST anomalies (Putrasahan et al., 2019; Hu and Fedorov, 2020; Lohmann et al., 2021). Moreover, DWF 90 has been connected to so-called cold air outbreaks (CAOs), i.e. transient weather events during which the ocean is significantly warmer than the atmosphere (Papritz et al., 2015; Papritz and Spengler, 2017; Papritz and Grams, 2018; Holdsworth and Myers, 2015). Observational data suggest that heat fluxes during CAOs play a central role for buoyancy reduction of surface waters in DWF sites (Svingen et al., 2023).



95 The objective of this study is to illuminate the processes involved in the formation of the NAWH downstream of large-scale
forestation and deforestation across North America. Given the strong sensitivity of the North Atlantic Ocean to climate forcing,
we test the hypothesis that forest cover changes over the upstream continent, i.e. North America, play a crucial role for the
formation of the NAWH. More specifically, we investigate the following research questions:

- How sensitive is the North Atlantic Ocean to upstream forest cover changes in comparison to global forest cover changes?
- 100 – How do our results fit into the context of previous findings on the NAWH which have mainly focused on the forcing of
anthropogenic climate change on the ocean?
- What mechanisms related to both buoyancy and wind forcing play a role in modulating the North Atlantic Ocean circu-
lation in North American forestation and deforestation scenarios?
- How does a regional warming or cooling on land propagate downstream over the ocean and shape the response of the
ocean circulation?

105 To answer these questions, we analyse fully coupled Earth system model simulations performed with CESM version 2 featur-
ing preindustrial CO₂ levels, in which vegetation-sustaining areas are either fully forested or deforested north of 30° N latitude
over the North American continent. Moreover, we perform Lagrangian trajectory analysis to trace the signal propagation from
North American land into the North Atlantic Ocean. The manuscript is structured as follows: First, we introduce the setup
of our forestation and deforestation experiments and the methods needed for the analyses in Sect. 2. We structure our results
110 into the comparison of the climate response to North American forest cover changes to global forestation scenarios previously
published by Portmann et al. (2022) in Sect. 3.1, the mechanisms controlling the buoyancy forcing in Sect. 3.2, the trajectory
analysis in Sect. 3.3, and lastly the impact of wind forcing on the ocean in Sect. 3.4. The results are summarized and discussed
in Sect. 4, complemented by ideas for further research.



2 Methods

115 2.1 Model setup

This study is based on simulations using CESM version 2.1.2 (Danabasoglu et al., 2020), using the Community Atmosphere Model (CAM6) and the Community Land Model (CLM5), the Parallel Ocean Program (POP2), the Los Alamos National Laboratory Sea Ice model (CICE5), and the hydrological routing Model for Scale Adaptive River Transport (MOSART). We perform three simulations: a pre-industrial control run, hereafter referred to as *control*, a forested run, *forestNA*, and a deforested run, *grassNA*. The implementation of the forest cover changes is the same as in Portmann et al. (2022), first developed by Davin et al. (2020): Vegetation-sustaining areas are forested for *forestNA* while all pre-industrial vegetation is converted to grassland in *grassNA*. In contrast to the approach in Portmann et al. (2022), forestation and deforestation are confined to North America taken as all ice-free grid points between 30°N and 85°N and between 170°W and 50°W (Fig. B1a, b). The implementation of forest cover changes is of idealised nature, as it does not take present-day land use into account. Therefore, the large croplands in North America are fully forested in these simulations. It should thus not be considered as a realistic forestation scenario (such as Griscom et al., 2017; Bastin et al., 2019; Mo et al., 2023), but as an idealised forestation experiment confined to a specific region in favor of exploring the governing mechanisms of the climate response.

In *forestNA*, areas with especially high forest cover changes are located from Alaska to northern Quebec, Newfoundland and Labrador, and the Great Plains (Fig. B1a). North American deforestation is most pronounced on the northwestern coast, and in a band north of the Great Plains up to southern Quebec and the north western USA (Fig. B1b). Atmospheric CO₂ concentrations are held constant at pre-industrial levels to isolate the biogeophysical effects of forest cover changes in opposition to carbon cycle effects. The land model is run in the dynamical biogeochemistry mode. Therefore, forestation does not always translate into mature trees in especially dry (e.g. Great Plains) or cold (e.g. Arctic islands) regions. Therefore, we show mean canopy top height 50 to 300 years after model initialization as an indicator of realized forest cover changes (Fig. B1c, d). Note also that boreal regions are largely populated by shrubs (compare Portmann et al. (2022) Supplement Fig. 1), which are also removed in *grassNA*. This leads to a notable increase in albedo without large changes in forest cover or canopy height (Fig. B1f).

The simulations are performed at a horizontal resolution of 1°. The three aforementioned experiments are branched off from a 1000-year pre-industrial control run after 200 years of spin-up time and subsequently run for 300 years. We note that the North Atlantic is anomalously fresh and cold with large AMOC variability (around -3 to +4 standard-deviations – not shown) at and around the branching point. This could bias the sensitivity of the North Atlantic to forest cover changes, but is assumed to be of minor importance as the climate response to forest cover changes is shown to be larger than this variability (Fig. 2). In addition, another forestation simulation branched off 50 years later features a similar, if not faster AMOC response (not shown). The following results are presented for the years 50 to 300 of the experiments and are referred to as the long-term response, unless otherwise stated.



145 2.2 Buoyancy flux decomposition

The buoyancy of ocean water, given by $-g\rho$ (g the acceleration of gravity and ρ density) is modulated by salinity and temperature (Gill, 1982). Less dense waters are hence more buoyant and a positive buoyancy flux anomaly (here defined positive upwards) means water becomes more buoyant. In this study, buoyancy flux is given in kg m^{-2} per year. To connect near-

150 Ocean salinity changes result from freshwater fluxes and temperature changes from heat fluxes through the ocean surface. The buoyancy flux into or out of the ocean B thus reads

$$B = B_H + B_{FW} = \frac{\alpha}{c_p^{water}} Q + \beta \rho_S \cdot S \cdot F_{FW}, \quad (1)$$

with B_H the buoyancy flux related to heat and B_{FW} the flux related to freshwater. The heat-related flux is given by the thermal expansion coefficient $\alpha = -\rho^{-1} \frac{\partial \rho}{\partial T}$, the specific heat content of water c_p^{water} , and the heat flux Q . The freshwater-related
155 buoyancy flux is the product of the haline contraction coefficient $\beta = \rho^{-1} \frac{\partial \rho}{\partial S}$, the density of salt water ρ_S , and the sea surface salinity (SSS) S with the fresh water flux F_{FW} (Pellichero et al., 2018). We assume c_p^{water} and ρ_S to be constant to simplify and speed up the computation of the buoyancy fluxes. Regarding the haline and thermal expansion coefficient, Gelderloos et al. (2012) found a feedback of the thermal expansion coefficient on the decline of AMOC during the Great Salinity Anomaly from 1968 to 1971, which is why we compute α and β as functions of local salinity, temperature, and sea level pressure according
160 to IOC et al. (2010) using the `gsw-python` library (McDougall and Barker, 2011).

We separate radiative (B^{rad}), turbulent (B^{turb}), and extracted heat due to snow- and ice-melt including latent heat-related (B^{meltH}) components to the heat-related contributions to the buoyancy flux. The freshwater-related flux is split into a flux resulting from ice melt (B^{ICEFW}) and one containing the fluxes from precipitation (containing snow), evaporation, and river runoff (B^{PERO}). The detailed computation of these fluxes from model output variables can be found in the Appendix Sect. A1.
165 For the analysis of buoyancy fluxes we use monthly averaged model outputs.

2.3 Identification of Cold Air Outbreaks

CAOs are events of a positive temperature difference between the ocean surface and the overlying atmosphere. These events lead to a large heat flux from the ocean to the atmosphere, ocean cooling, and subsequently DWF (Holdsworth and Myers, 2015; Papritz et al., 2015). We identify CAOs similarly to Papritz and Grams (2018) as grid-cells where the difference $\Delta\theta$
170 between potential skin temperature θ_{SKT} and potential temperature at 850 hPa θ_{850} is larger than 0 with $\Delta\theta = \theta_{SKT} - \theta_{850}$. Using skin temperature is beneficial since it is also defined over ice. It is computed as:

$$\theta_{SKT} = T_S \left(\frac{p_{ref}}{p_S} \right)^{\left(\frac{R}{c_p^{air}} \right)} \quad (2)$$

Here, T_S is the surface temperature given by the model output in K, $p_{ref} = 1000$ hPa, p_s surface pressure in hPa, $R/c_p^{air} = 0.268$ with R the gas constant in $\text{J mol}^{-1} \text{K}^{-1}$, and the specific heat of air c_p^{air} in $\text{J kg}^{-1} \text{K}$. Since CAOs are often short-
175 lived, they are identified using 6-hourly atmospheric model output. Similar to Papritz and Spengler (2017), CAO regions are



categorized according to the magnitude of $\Delta\theta$ in $(0, 4]$, $(4, 8]$, $(8, 12]$, and > 12 K. The resulting CAO masks include for example the center of a CAO of 9 K in the $(4, 8]$ K category while the surrounding areas are attributed to the weaker categories.

These binary CAO masks are subsequently used to mask heat fluxes. Summing up the heat fluxes associated with CAOs and dividing them by the total upward heat flux in the Labrador Sea (here defined from from 52°N to 65°N and from 45°W to 65°W (see also black box in Fig. 3m) results in the fraction of positive upwards heat flux associated with CAOs with respect to the total heat flux. Moreover, the resulting two-dimensional fields are used to identify potential target regions for trajectory analysis in Sect. 3.3. For the trajectory analysis, we refer to CAOs with $\Delta\theta \leq 8$ K as weak CAOs, while CAOs with $\Delta\theta > 8$ K are referred to as strong CAOs.

2.4 Trajectory analysis

Lagrangian air parcel trajectories are computed to trace the impact of land cover change on the ocean using 6 hourly model output. 5-day backward trajectories are started every 12 hours, 100 km apart, and 100 hPa above the ground in the Labrador Sea where $\Delta\theta = \theta_{SKT} - \theta_{850} > 0$ K. The extent of the Labrador Sea and thereby target region is defined as in Sect. 2.3. Land areas are excluded from the starting points. We post-process the trajectories, filtering out trajectories with a $\Delta\theta$ below the CAO threshold, since some trajectories might be started outside the masks due to grid interpolation. The trajectories are computed using Lagranto version 2.0 (Sprenger and Wernli, 2015) adapted to use CESM output. For this analysis, 6-hourly model output from the years 150 to 200 is used. We restrict this analysis to 50 years to reduce computational costs since we do not expect a qualitative change of our results by including more years. The window of years 150 to 200 is a time period of relatively stable AMOC strength in both *forestNA* and *grassNA* (Fig. 2c). Along the trajectories, several variables are traced: potential temperature of the air parcel, potential skin temperature below the trajectory and net surface turbulent heat fluxes.

Starting trajectories in CAO regions in the Labrador Sea allows to trace the impact of land cover change on the ocean circulation through the effect on the connecting air parcels. The evolution of the traced variables from CAO trajectories is compared between *forestNA* and *grassNA* for strong and weak CAO target regions. Normalized trajectory densities are first presented in Sect. 3.3 following the approach of Schemm et al. (2016) and are calculated as $\frac{n_i}{N_t \text{area}_i} \cdot 100$ with n_i the number of trajectories associated with a certain grid-cell i , N_t the total number of trajectory existing at timestep t , and area_i the area of the concerned grid-cell. The unit of the density is $\% \text{ km}^{-2}$.

2.5 Wind-driven streamfunction

To estimate the effect of wind stress changes on the direction of the oceanic flow, we calculate a simple approximation of the wind-driven flow using the Sverdrup relation (Sverdrup, 1947),

$$V_{Sv} = \frac{1}{\rho_0 \beta} \nabla \times (\boldsymbol{\tau}), \quad (3)$$

where V_{Sv} is the depth-integrated meridional transport, ρ the density of sea water, β the Rossby parameter in $\text{m}^{-1} \text{s}^{-1}$, and $\boldsymbol{\tau}$ surface wind stress in Pa from model output. This is then zonally integrated from the eastern boundary to yield a streamfunction related to wind stress forcing. We note that this can only provide a very rough estimate and should not be over-interpreted since



Sverdrup balance is not fully accurate in the subpolar North Atlantic (Wunsch and Roemmich, 1985; Yeager, 2015). While more sophisticated approaches exist (e.g. Chen et al., 2022), we follow other previous studies for comparability (Putrasahan et al., 2019; Lohmann et al., 2021; Ghosh et al., 2023).

3 Results

First, the long-term response of surface variables and AMOC to North American forestation and deforestation are described. These are related to the global-scale simulations discussed in Portmann et al. (2022) to investigate the sensitivity of the North Atlantic to upstream forest cover changes. Moreover, similarities and differences of the found long-term response to anthropogenic warming simulations are explored. This is followed by a more in-depth analysis of air-sea interactions which are grouped into thermodynamic (including CAOs) processes and the trajectory analysis, followed by the mechanical processes (wind stress).

3.1 Response of near-surface temperature, wind, and the Atlantic Meridional Overturning Circulation

We find that North American forestation warms global mean near-surface temperatures by 0.09 K while deforestation cools it by 0.52 K (Fig. 1a, b). As expected, the temperature changes is most pronounced over North American land. However, the North Atlantic near-surface temperatures cool by more than 4 K regionally in *forestNA* and warm by up to 1 K in *grassNA*. In *forestNA*, the negative anomaly near the North Atlantic ocean surface extend downstream over Europe and even further downstream over parts of Asia. The impact of forestation on the Northern Hemisphere surface temperature is confined to North American land. In contrast, parts of the Southern Hemisphere ocean exhibit a slight warming response. This points towards a decrease in meridional overturning and thus less equatorward heat export from the Southern Ocean (Rahmstorf, 2024; Armstrong McKay et al., 2022). In contrast, deforestation cools the Northern Hemisphere and large parts of the Southern Hemisphere. Cooling is most pronounced over the deforested areas. Similar as for *forestNA*, the response of the Southern Hemisphere in *grassNA* is likely related to an increase in equatorward ocean heat transport further described below.

Naturally, the global mean temperature response is weaker when limiting forest cover changes to North America compared to global forestation (Portmann et al., 2022). In Portmann et al. (2022), global forestation was shown to increase global mean near-surface temperatures by 0.49 K and deforestation to decrease it by 1.58 K (comparison to Portmann et al., 2022 Fig. 1a, b). Moreover, the temperature response over North American land is also weaker, most likely due to reduced advection of anomalously warm/cold air from Asia to North America. Meanwhile, the response in the North Atlantic SSTs is remarkably similar. The warming hole in *forestNA* is of similar spatial extent and magnitude as the warming hole in response to global forestation. The cooling hole in *grassNA* is weaker compared to global deforestation, but of similar spatial extent. This shows that forest cover changes over North America alone are sufficient to result in a negative North Atlantic SST anomaly similar to global forest cover changes (Portmann et al., 2022). This points towards an enhanced sensitivity of the North Atlantic ocean to upstream land cover changes.



A qualitative comparison of the *forestNA* warming hole to the NAWH found in observations (Rahmstorf et al., 2015; He et al., 2022; Gervais et al., 2018) shows that the NAWH in *forestNA* is more pronounced in the Labrador Sea instead of having its greatest anomaly in the central North Atlantic. Indeed, the location and spatial extent of the observed warming hole are more similar to that of the cooling hole in *grassNA*. This is also true in comparison to the projected NAWH at the end of the 21st century under a high emission scenario (RCP8.5) where the greatest magnitude of the NAWH is shifted to the east of Greenland (Menary and Wood, 2018) instead of the Labrador Sea. This raises the question why the warming hole in *forestNA* is shifted into the Labrador Sea compared to the SST anomaly visible in *grassNA* as well as anthropogenic warming observations and projections. This is further explored in Sect. 3.2.

Compared to global forestation and deforestation (Portmann et al., 2022), near-surface wind speed changes are almost identical over North American land. Forestation decreases near-surface wind speed in the north, from Alaska to Quebec, by up to 1 ms^{-1} (Fig. 1c). In central North America we see a positive wind anomaly, as in Portmann et al. (2022), the cause of which is not entirely clear. Potentially, this very dry region is not sustaining the afforestation and thus simulates less roughness than the vegetation in *control* (most likely crops or grass) which agrees with the absence of significant changes in canopy height in this region (Fig. B1c). Moreover, orographic effects downstream of the Rocky Mountains in combination with changes in thermally-driven circulation could influence this response. However, the impact of these changes is local and it is reasonable to assume that this increase in wind speed has only a weak downstream influence on the North Atlantic. It is beyond the scope of this study to investigate this local change in the wind speed. In contrast, deforestation leads to a significant increase of near-surface wind speeds over North America, with the strongest increases located in the northeast (Fig. 1d). Locally, wind speed increase can exceed 2 ms^{-1} . Similarly, over the warming hole region in *forestNA* wind speed decreases while in *grassNA* it increases, which is potentially related to the SST anomalies as further discussed in Sect. 3.4.

In this study, AMOC strength is quantified as the maximum of the zonally averaged meridional overturning streamfunction between 20°N and 70°N and below 500 m (AMOC index, Liu et al., 2020; Portmann et al., 2022). The median AMOC strength during the years 50 to 300 declines in *forestNA* by 12 % or 2.0 Sv to a median of 20.6 Sv, while it increases in *grassNA* by 20 % or 4.7 Sv to 28.1 Sv (Fig. 2c). In comparison, global forestation weakens AMOC by 22 % in Portmann et al. (2022) and deforestation strengthens it by 49 %. Thus, while we find a warming hole of similar intensity in *forestNA* compared to global forestation simulations, the AMOC reduction is less pronounced. This shows that the strength of the warming hole does not depend linearly on the AMOC strength, corroborating the findings from Keil et al. (2020). That the responses of the AMOC and SSTs to forestation and deforestation are nonlinear can be linked to a sea ice feedback as discussed in Sect. 3.2. However, further factors like shortwave cloud feedbacks or export of water towards higher latitudes might also play a role here (Keil et al., 2020).

The zonal average of the overturning circulation (i.e., the AMOC streamfunction) decreases in *forestNA* in almost the entire basin, albeit a positive anomaly at 60°N suggesting a shift of the streamfunction to the equator (Fig. 2a). This shift can also be seen in the contours. Moreover, overturning becomes more shallow. In *grassNA*, changes are of the opposite sign and stronger compared to *forestNA* (Fig. 2b). In height coordinates, the AMOC intensifies and deepens. The maximum anomaly in comparison to *control* is shifted to a greater depth than in *forestNA*. For both *forestNA* and *grassNA*, changes in the zonally

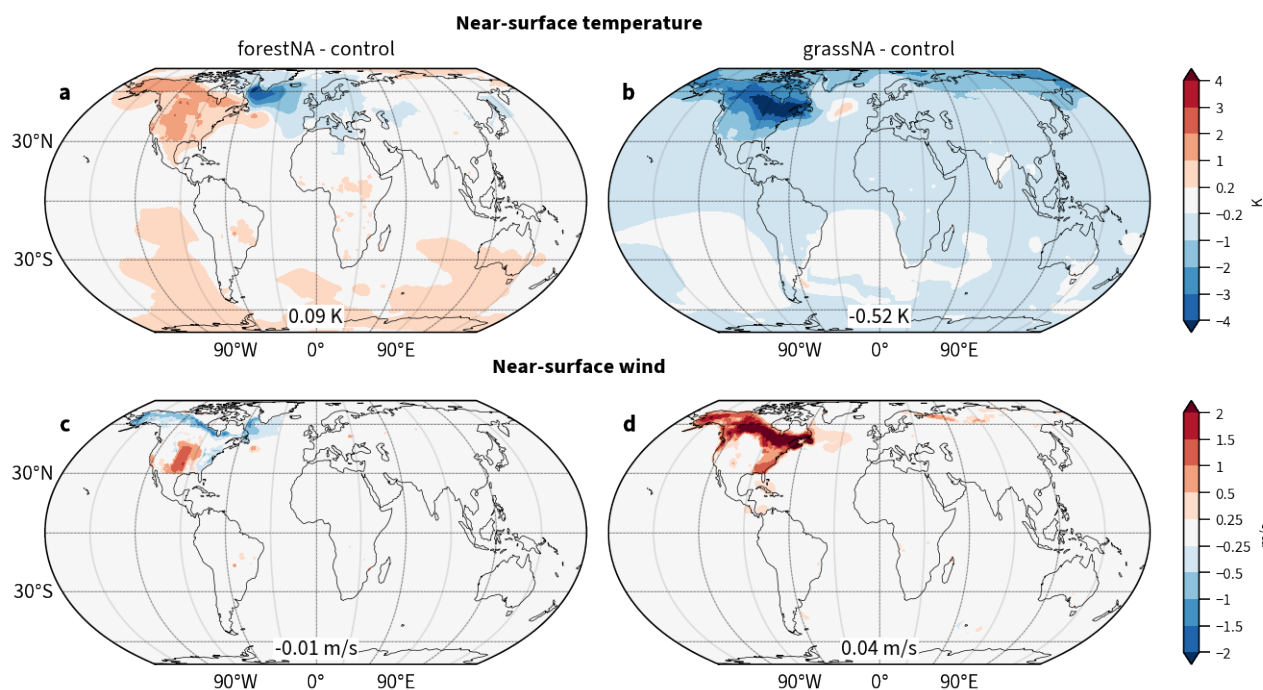


Figure 1. (a), (c) Global response of near-surface temperature (b), (d) and near-surface wind to forestation (*forestNA-control*) and deforestation (*grassNA-control*) over North America. Shown is the average over the years 50 to 300 of the corresponding simulation relative to *control*. Numbers in boxes indicate globally averaged changes.

averaged AMOC are weaker and shallower compared to global forest cover experiments (Portmann et al., 2022). Similar to
 275 Portmann et al. (2022), AMOC changes are computed in potential density coordinates (Fig. B2) which, in line with the global
 simulations, shows that AMOC maxima and their changes occur further poleward. Note that the overshoot of the AMOC index
 during the first 70 years of *control* relates to model-specific sea ice variability (Danabasoglu et al., 2020). While the AMOC
 index of *control* remains within the variability of the last 500 years of the longer control simulation (grey range in Fig. 2) it was
 branched off of, *forestNA* and *grassNA* mostly lie outside that range after year 50. In the context of anthropogenic warming, the
 280 annual mean AMOC response to North American forestation is weaker compared to that projected in RCP8.5 global warming
 scenarios for which Rahmstorf et al. (2015) project a decrease of up to 8 Sv and Liu et al. (2020) a decrease of 10 Sv. For a
 halving of 1950 wind stress, Lohmann et al. (2021) find a stronger weakening of the AMOC with similar vertical structure as
 in *forestNA*, albeit no equatorward shift. Conversely, when doubling the wind stress they observe a shift of the AMOC to a
 greater depth (with positive anomalies close to the surface) instead of only a strengthening and deepening as in *grassNA*. The
 285 role of wind stress in our simulation is discussed in more detail in Sect. 3.4.

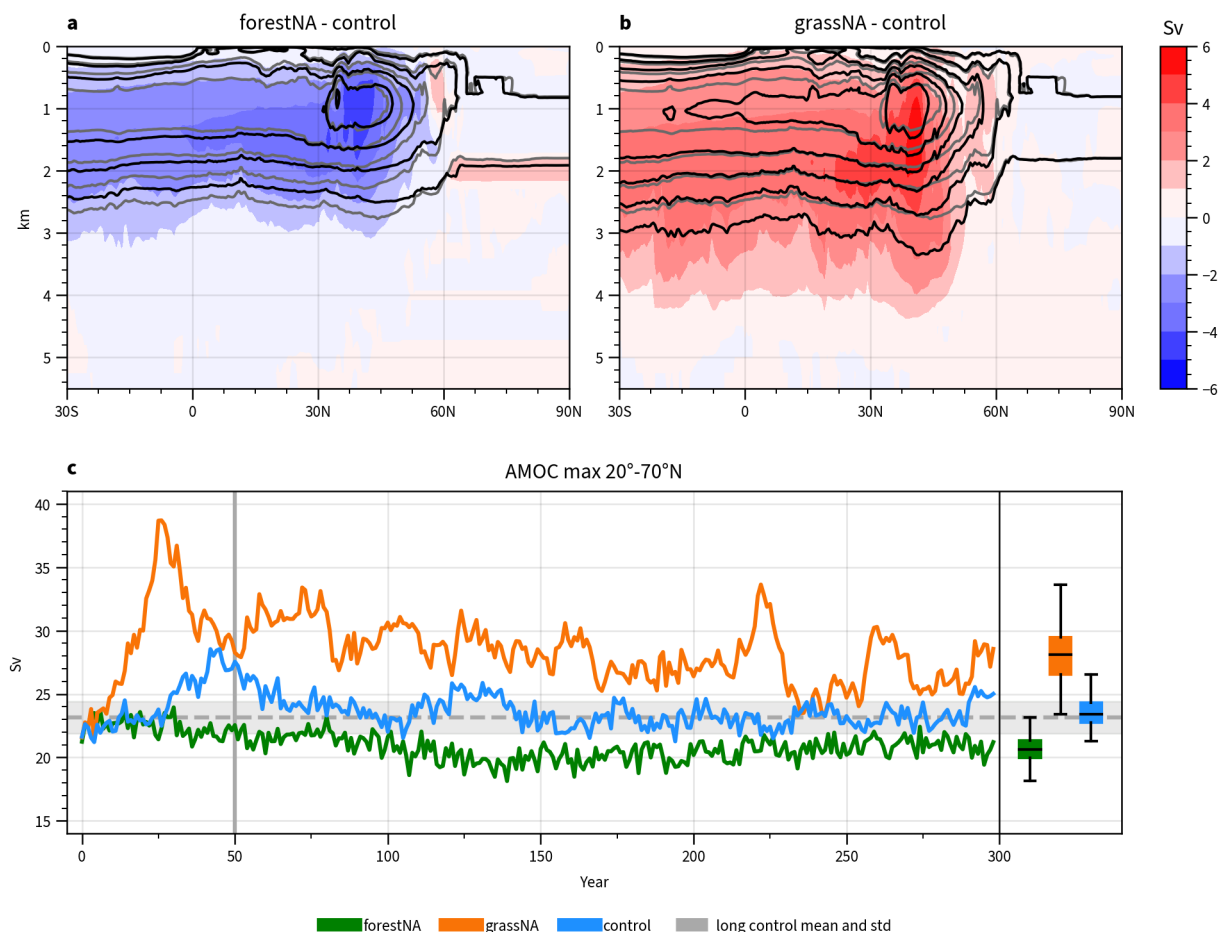


Figure 2. Depth profile of changes in the zonally averaged overturning streamfunction for (a) *forestNA* and (b) *grassNA* for years 50 to 300. Shading represents scenario differences with respect to *control* in steps of 1 Sv. Contours show absolute values in steps of 4 Sv starting at 4 Sv for *forestNA* and *grassNA* in black and in grey for *control*. (c) Time evolution of the AMOC index for *forestNA* (green), *grassNA* (orange), and *control* (blue). In grey, the mean and standard deviation of the AMOC index of the second half of the 1000-year long control run is shown. The box-plots summarize the evolution over the years 50 to 300 for *forestNA* (green, left), *grassNA* (orange, middle) and *control* (blue, right). Black lines indicate the median while boxes show the interquartile range. Values outside of 1.5 times the interquartile range are treated as outliers. The vertical grey lines mark the year 50 and 300.



3.2 Mechanisms driving density changes

In this section, we turn to the mechanisms involved in forming the SST response through density changes of the ocean waters. Forest cover changes over North America lead to significant changes in albedo (Fig. B1e, f) and temperature (Fig. 1). Changes in albedo are strongest in a narrow band spanning from Alaska (70°N) to Quebec (50°N), with less albedo changes north and south of this band in accordance with changes in canopy height (Fig. B1c, d) and reduced snow albedo feedback further equatorward. Overall, this indicates that there is a very narrow high latitude band where the pre-industrial control climate responds strongly to forest cover changes in agreement with previous studies (Wang et al., 2014; Betts, 2000; Asselin et al., 2022).

To discuss the long-term response of the ocean circulation to the imposed North American land cover changes, we focus on the winter half year (December to May i.e. DJFMAM). This choice is justified firstly since the albedo response is the strongest during winter and spring (Fig. B3, Davin et al. (2020); Jiao et al. (2017)). This is true especially in the high latitudes due to trees dampening the high albedo of snow. Secondly, the winter half year is the period during which the North Atlantic ocean circulation is most sensitive to atmospheric forcing (Luo et al., 2014; Guo et al., 2024); on the one hand, ocean water cools over the winter and is subsequently the coldest in spring and, on the other hand, sea ice formation during the winter leads to enhanced salt content in spring, making the waters the most dense in this season. Thus, DWF driving the AMOC is most intense in spring (Svingen et al., 2023). This temporal concurrency of the largest impact of vegetation changes and ocean sensitivity likely favors a large response of the ocean to land cover changes.

The cold SST anomaly in *forestNA* (Fig. 3a) is collocated with the anomaly in near-surface air temperature in (Figure 1a). It is strongest around the tip of Greenland and covers the whole Labrador Sea west of Greenland. The SST anomaly stretches beyond Iceland in the north and eastward towards the European coast with a greater intensity towards the southeast. In contrast, the warm SST anomaly in *grassNA* is strongest in the central North Atlantic with only a thin branch into the Labrador Sea and Davis Strait (Fig. 3b). Both simulations show strong anomalies of opposite sign (warm in *forestNA* and cold in *grassNA*) east of Nova Scotia. The pattern of a cold temperature anomaly in the North Atlantic with a warm anomaly east of Nova Scotia is also known from observations (Rahmstorf, 2024; Caesar et al., 2018; Zhang and Vallis, 2007) and part of an SST pattern also referred to as the SST fingerprint in response AMOC changes.

Mixed layer depth and sea ice

The Labrador Sea is a region of intensive DWF, which plays a significant role in driving the AMOC and the NAWH (Böning et al., 2023; Garcia-Quintana et al., 2019; Gervais et al., 2018; Kuhlbrodt et al., 2001). A common measure for DWF is the mixed layer depth (MLD). MLD in this section is defined as the depth of the maximum buoyancy gradient. In *forestNA*, the negative SST anomaly overlaps with a strong MLD anomaly (Fig. 3 c.). The reduction in MLD is most pronounced in the Labrador Sea with extensions east of Greenland and in the southeastern North Atlantic. The negative MLD anomaly is collocated with sea ice growth in the Labrador Sea (Fig. 3c). With DWF mitigated, the AMOC is weakened and less warm water is imported into the Labrador Sea, facilitating sea ice growth. The advancing sea ice insulates the ocean from the atmosphere,

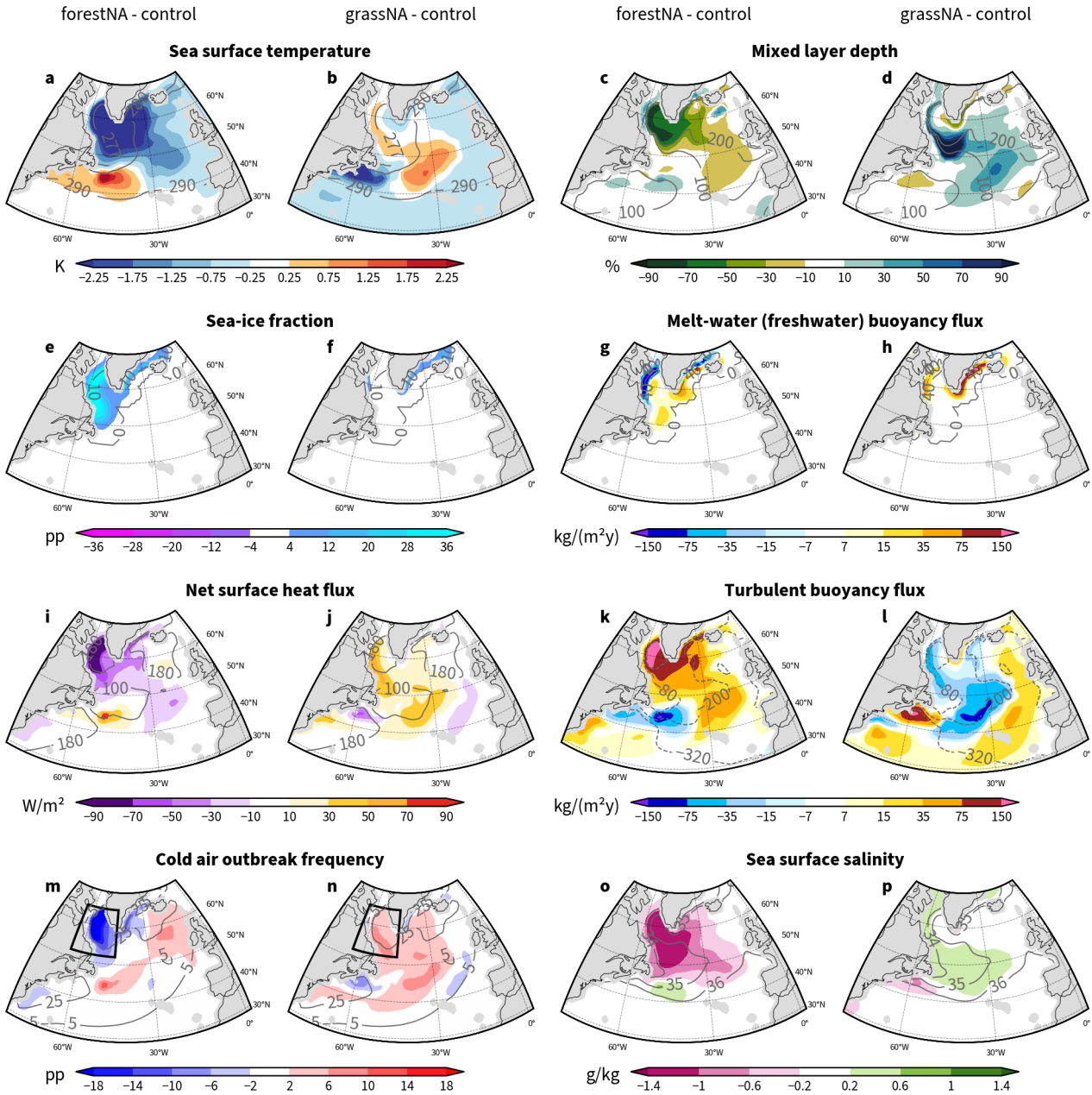


Figure 3. Average changes of DJFMAM response to forestation (left) and deforestation (right) from the years 50 to 300 of the simulations for (a), (b) SSTs, (c), (d) MLD, (e), (f) sea ice fraction, (g), (h) melt-water (freshwater) buoyancy flux $B^{ICE_{FW}}$, (i), (j) upward turbulent heat fluxes, (k), (l) turbulent buoyancy fluxes B^{turb} , (m), (n) frequency of cold air outbreaks $\Delta\theta > 4K$, and (o), (p) sea surface salinity. In panels (g), (h), (k), and (l), positive buoyancy flux anomalies lead to more buoyant surface waters. Grey contours depict absolute values of control. Black boxes in (m) and (n) signify the Labrador Sea extent used for analyses in Fig. 4 and Sect. 3.3. Note the non-linear color shading intervals in (g), (h), (k), and (l).



hindering the ocean from losing heat and further inhibiting DWF. This feedback cycle is rather slow and weakens AMOC
320 gradually over time as seen in Fig. 2c, as sea ice grows slowly over several decades.

In addition to cutting off the heat loss to the atmosphere, as the sea ice edge advances, melt-water fluxes shift further toward
the open ocean as well (Fig. 3g). Enhanced melt-water fluxes increase the buoyancy of the waters and thus dampen vertical
mixing. Buoyancy due to freshwater from melt-water fluxes increases in the Labrador Sea and east of the tip of Greenland.
In contrast, buoyancy decreases locally around the *control* sea ice edge as melt-water and thus fresh water fluxes are missing
325 there. This is why we see also small increases in MLD along the *control* sea ice edge (Fig. 3e, c).

Sea ice model output confirms that the increase in sea ice is driven by a local SST decrease and not by increased import by
wind (not shown). This rules out the hypothesis that wind changes are responsible for the the growth of sea ice extent (Schemm,
2018); the net sea ice change by dynamics in the Labrador Sea was even found to decrease in *forestNA* despite the larger sea ice
extent compared to *control*. Note that due to the anomalously cold waters, Labrador Sea ice melt starts later in the year and we
330 see the largest freshwater fluxes shift into summer in *forestNA* (not shown). However, the increased freshwater buoyancy fluxes
from ice melting are largely compensated by the additional insulation of the ocean surface by the ice, where otherwise solar
radiation would be warming the upper levels of the ocean, manifesting in a negative heat buoyancy flux anomaly. Attempting
to compare these two buoyancy flux components is possibly complicated by cloud responses (Keil et al., 2020).

Similar to *forestNA*, the SST anomaly overlaps with a change in MLD in *grassNA* (Fig. 3d). Here, MLD increases over most
335 of the North Atlantic, with the greatest anomalies occurring around the tip of Greenland. The Northeastern Atlantic is another
location of large MLD changes, albeit of smaller magnitude than in the Labrador Sea. Compared to *forestNA* only a thin band
of anomalous MLD reaches into Davis Strait. This is due to the fact that cold temperatures in *grassNA* on land lead to increases
in sea ice along the coasts (Fig. 3f) and increasing freshwater fluxes there (Fig. 3d). This narrows the region of increased MLD
to the pattern we see in Fig. 3d. Sea ice anomalies are however small compared to *forestNA*. The increased import of warm
340 water by the AMOC in *grassNA* prevents sea ice from growing extensively. Since there is less shielding of the ocean from the
atmosphere by sea ice, AMOC reacts faster in *grassNA* (Fig. 2). The fact that the strongest changes in MLD do not overlap as
well with changes in SST in *grassNA* as they do in *forestNA* is to first order due do sea ice. In *forestNA*, anomalies in MLD and
SST are strongest where sea ice is insulating the ocean. This insulation acts to slow down AMOC, which influences SSTs in
the whole of the North Atlantic by reduced warm water import.

The same SST and MLD patterns as in *grassNA* have been found for anthropogenic warming experiments in Gervais et al.
(2018) albeit with opposite sign. Using CESM, they also find that under an RCP8.5 scenario, the Arctic will be ice-free at the
end of the 21st century. Correspondingly, freshwater from melting ice is the main driver of a reduction in DWF at the beginning
of their simulations. In our simulations it seems the warming over land is not strong enough to induce widespread melting. As
a consequence, a feedback loop of reduced DWF, cooling SSTs and enhanced insulation of the ocean from the atmosphere by
350 sea ice and thus reduced heat loss lead to the cooling pattern over the North Atlantic observed in *forestNA*. Note that in our
simulations, the dynamic time evolution of the Greenland ice sheet is disabled to decrease the complexity of the problem. It
is possible that warming from forestation would prompt the Greenland ice sheet to melt and make the North Atlantic waters
even more buoyant, thereby accelerating AMOC decline (Martin et al., 2022). Moreover, the North Atlantic is anomalously



fresh and cold at the branching point, which makes a strong reaction of sea ice in *forestNA* more likely. However, significant
355 *forestNA* sea ice growth only happens after about year 100 onwards (not shown), speaking against this hypothesis.

Overall, sea ice growth is a key factor in dictating the location, extent and magnitude of the SST anomalies in the North Atlantic. Anomalous sea ice growth due to a slowdown in AMOC is the reason why the simulated NAWH in *forestNA* is more intense in the Labrador Sea compared to what is found in observations, where the warming hole is shifted more into the central North Atlantic, similar to the cooling hole in *grassNA* (Rahmstorf et al., 2015; He et al., 2022; Gervais et al., 2018). Moreover,
360 it is likely also the reason why the warming hole in *forestNA* is of similar strength to the one found in the global forestation experiment of Portmann et al. (2022). The sea ice response depends heavily on the local cooling close to the North American coast and thus leads to similar sea ice extent (not shown) and surface cooling in both simulations. Similarly, in *grassNA*, the absence of anomalous sea ice growth leads to a NACH with a similar spatial pattern as in anthropogenic warming simulations.

Heat fluxes and cold air outbreaks

365 Addressing the driving mechanism for the reduced vertical mixing in the DWF regions, we find that turbulent air-sea heat fluxes are the main driver of buoyancy changes (Fig. 3i, j). In *forestNA*, the turbulent heat fluxes decrease strongly under the sea ice and negative net heat flux anomalies extend into the central North Atlantic. For both, *forestNA* and *grassNA*, changes in turbulent buoyancy fluxes induced by net surface heat flux changes dominate the anomalies in total buoyancy fluxes in the whole North Atlantic except in close proximity to the *control* sea ice edge (Fig. 3k, l and Fig. B4). Consequently, the changes
370 in turbulent buoyancy fluxes are of larger importance than (sea ice) melt-water or other buoyancy fluxes, with the exception of the coastal regions. For both runs, turbulent heat flux anomalies are greatest in the Labrador Sea with sensible heat fluxes dominating over latent heat fluxes (not shown).

Several studies in the past have found that air-sea heat fluxes and subsequently DWF in the North Atlantic are heavily dependent on CAOs (Svingen et al., 2023; Papritz and Spengler, 2017; Renfrew et al., 2023). Similar to Papritz and Spengler (2017)
375 and Svingen et al. (2023), who focused their studies on the Irminger and Nordic Seas, and the Greenland Sea, respectively, we find that up to 80 % of heat flux extraction from the Labrador Sea occurs during CAOs (Fig. 4a). Our results show that the number of CAOs with $\Delta\theta > 4K$ in *forestNA* decreases in the Labrador Sea (Fig. 3m) and so does the total area covered by CAOs (Fig. 4b). Conversely, in *grassNA*, CAOs increase over the Labrador Sea but also the central North Atlantic (Fig. 3n). In both cases, changes in strong CAOs ($\Delta\theta > 8K$) dominate the response in the Labrador Sea, while weaker CAOs respond
380 more strongly over the open ocean (not shown). Subsequently, the heat flux associated with CAOs in *forestNA* decreases to almost a third of that in *grassNA* (Fig. 4c) while the fraction of positive heat flux extracted during CAOs compared to times without CAOs only decreases marginally (Fig. 4a). This means in both scenarios CAOs are the main driver of heat extraction from the ocean: In *forestNA* CAOs are becoming less frequent and less strong, mitigating heat transfer to the atmosphere while the opposite is true for *grassNA*.

385 Such a result is also reflected in the evolution of integrated turbulent heat fluxes and MLD during CAOs: changes in MLD overlap well with the integrated ocean-to-atmosphere heat flux associated with strong CAOs (Fig. 4d–g) starting from February onwards. First, weak CAOs continuously extract heat from the ocean from November to December and no mixed layer

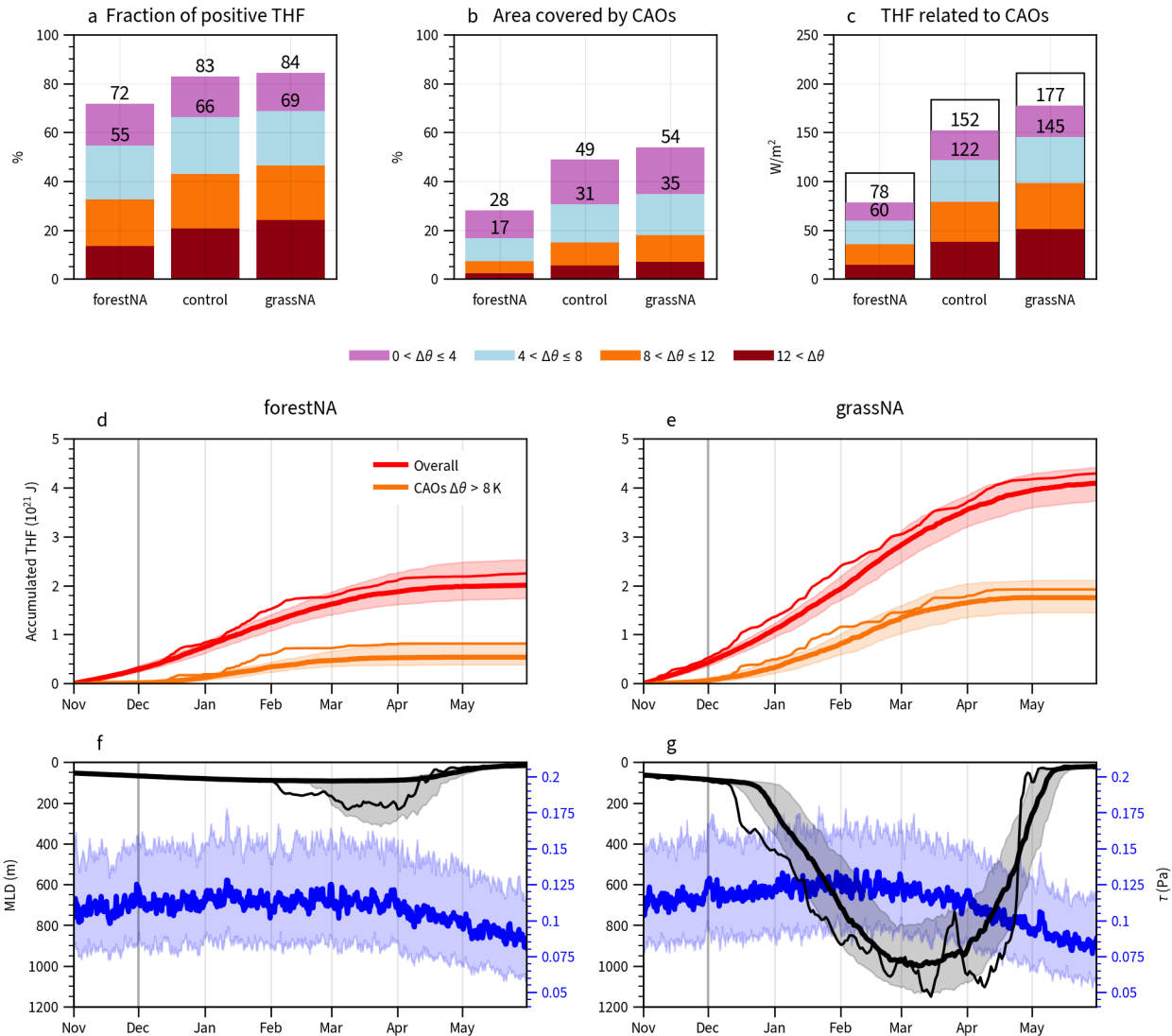


Figure 4. CAO statistics in the Labrador Sea (extent as drawn in Fig. 3m, n) over the years 50 to 300. **(a)-(c)** are for DJFMAM. **(a)** Relative fraction of upward turbulent heat flux associated with the different CAO categories with respect to all upward turbulent heat fluxes in the season (i.e. a value of 100% would indicate that all upwards turbulent heat flux in the Labrador Sea is occurring during CAOs), **(b)** the area covered by CAOs (equal to the frequency, i.e. fraction of time steps that experience a CAO), and **(c)** the absolute values of the turbulent heat fluxes associated with CAOs. Categories are according to the potential temperature difference $\Delta\theta$ in colors and transparent if below zero (i.e. the ocean taking up heat from the atmosphere) **(c)**. For a given threshold $\Delta\theta$, the associated quantity is given by the sum of the categories above the threshold, corresponding to the sum of all the bars underneath and including the respective threshold. Numbers denote the sums for CAOs of strengths greater than $\Delta\theta > 0$ K and $\Delta\theta > 4$ K, respectively. **(d), (e)** Average accumulated turbulent heat flux overall in red and only within in strong CAOs ($\Delta\theta > 8$ K) in orange over November to the end of May for *forestNA* and *grassNA*. **(f), (g)** Similarly, average MLD in black and wind stress τ in blue. Heavy lines represent the medians and shading the interquartile ranges. In **(d)-(g)**, thin lines depict the year 148 as a case study (randomly selected), except for wind stress. Vertical grey lines in **(d)-(g)** mark the start of December.



390 deepening is observed. Only when stronger CAOs extract a lot of heat in short periods of time from January to March does the mixed layer deepen. Starting from around February, strong CAO events push the MLD deeper while mild CAOs presumably maintain the MLD, as described by Svingen et al. (2023). In *forestNA*, many of the simulation years do not experience mixed layer deepening below 100 m at all (Fig. 4f) since extracted heat flux from strong CAOs in spring stagnates (Fig. 4d). It is in agreement with the finding of Holdsworth and Myers (2015) that CAOs play a greater role in warmer years or a generally warmer climate to start DWF. In contrast, the extracted heat content is much higher in *grassNA* and so is MLD. These findings further support the hypothesis of a non-linear response of MLD to CAOs and extracted heat flux.

395 Note that the average magnitude of wind stress in the Labrador Sea, which could also account for enhanced vertical mixing on the CAO time scale, has a seasonal maximum around February when also the mixed layer deepens most. In line with Fig. 1d, wind stress is slightly larger in *grassNA* than in *forestNA*, such that the increased vertical mixing in *grassNA* compared to *forestNA* can be partially attributed to faster winds. However, compared to the changes in the accumulated turbulent heat flux, wind stress differences between the simulations are considered as small. The effect of wind stress changes on the subpolar gyre are discussed further in Sect. 3.4.

Salinity

In addition to temperature, salinity controls ocean water density. A higher salt content reduces buoyancy and vice versa. The salinity in the North Atlantic is controlled by freshwater fluxes, evaporation, and import from southerly regions through the ocean circulation (Born et al., 2016; Holdsworth and Myers, 2015). With less salt import, more buoyant waters lead to less DWF and thus reduced AMOC strength. This mechanism is known as salinity-advection feedback (Born et al., 2016). Sea surface salinity (SSS) in *forestNA* decreases most in the Labrador Sea, but also to a large extent in the entire North Atlantic, except for the region of positive temperature change east of Nova Scotia (Fig. 3o).

One could expect that the increased freshwater fluxes in the Labrador Sea away from the *control* sea ice edge would contribute to a reduced SSS in this region. However, this is not observed in the salinity anomaly, as the pattern is rather distinct from that of the freshwater buoyancy anomaly (Fig. 3g). Similarly, the change in precipitation, evaporation, and runoff buoyancy flux B^{PERO} is small over the whole North Atlantic and thus negligible for changes in salinity (Fig. B4g). In *grassNA*, the salinity anomaly is weaker than in *forestNA* and of smaller extent. SSS in *grassNA* increases in the Labrador Sea along Davis Strait and in the central North Atlantic, also not displaying a signature from freshwater forcing. We conclude the changes in SSS are thus not dominated by changes in freshwater fluxes but instead by the reduced salt advection from southern regions, amplified by and itself amplifying the AMOC strength reduction through salinity advection feedback.

Moreover, the salinity anomalies in the northeastern North Atlantic in *forestNA* and the central North Atlantic are likely the reason for the reduced MLD there, even though we see no strong response of CAOs in this region. The reduced import of salt through reduced AMOC leads to more buoyant waters and thus less DWF. Lohmann et al. (2021) find a salinity decrease of comparable strength in response to halving of wind stress, leading to a comparable AMOC decline. Similarly to their findings, the salinity-advection feedback in our study acts to enhance the AMOC changes induced by atmosphere-ocean interactions, i.e. changes in CAOs and associated ocean-to-atmosphere heat fluxes. As a consequence, the salinity-advection feedback merely



increases the magnitude and large-scale extent of the SST anomalies but is not the leading cause. This is in contrast to studies focusing on melt-water-induced changes in AMOC, where the salt-advection feedback is the direct trigger for changes in AMOC and subsequent SST response (van Westen et al., 2024; van Westen and Dijkstra, 2023).

425 However, the question arises how the sensitivity of the ocean to changes in the atmospheric forcing (CAOs and resulting ocean-to-atmosphere heat fluxes) is linked to the ocean salinity. We hypothesize that the salinity state is important for the effect of CAOs. At constant salinity, warmer temperatures lead to a higher thermal expansion coefficient α (Gelderloos et al., 2012; Suckow et al., 1995), thus a higher sensitivity of the ocean to temperature changes. In addition, the sensitivity to temperature is also enhanced at higher salinity (Suckow et al., 1995). Both combined, suggest a higher sensitivity to atmospheric forcing in
430 *grassNA*, where the North Atlantic is warmer and more salty (Fig. 3b, p). This aligns well with the faster AMOC response to atmospheric forcing in the beginning in *grassNA* and also the subsequent higher AMOC variability in *grassNA* (Fig. 2c) given the higher year-to-year variability of atmospheric temperatures (Hogan and Sriver, 2019). The importance of these mechanisms could be investigated by studying different Earth system models featuring different Labrador Sea salinity climatologies or by inducing changes in salinity through modified freshwater forcing in addition to atmospheric perturbations.

435 3.3 Trajectory analysis

In the previous section, the importance of CAOs for the heat exchange and thereby vertical stratification in the Labrador Sea was identified. However, one objective of this study is to link the changes in atmosphere-ocean interactions to the initial land cover perturbations. To close this gap, we next investigate backward air parcel trajectories started during CAOs in the Labrador Sea (region marked by the black boxes in Fig. 3m, n). On the one hand, this allows to identify the source regions of CAO air
440 masses. On the other hand, by tracing the evolution of several variables along these trajectories, we can disentangle the roles of changes of sea and air temperatures for heat flux intensities. This helps illustrating the causal pathway from impacts of land cover changes on the atmosphere to impacts of the atmosphere on the ocean.

24 hours before arriving at the target locations, the trajectories are still largely located above the Labrador Sea with the highest densities over Davis Strait, Quebec and east of Greenland (Fig. 5a–d). 96 hours before reaching their target location,
445 the trajectories spread further west- and poleward, hereafter also referred to as the CAO trajectory source regions (Fig. 5e–h). It is not surprising that the coldest trajectories in the Labrador Sea originate from the climatologically coldest regions like the high Arctic and North American boreal land. These regions are not necessarily regions with forest cover changes. This suggests that forest cover change does not only directly influence the air parcels upstream but does so by also influencing the surrounding regions. Thus, very high latitude forest cover changes also over Eurasia could lead to a similar ocean response as
450 in Guo et al. (2024) who found a similar cooling hole response as in *grassNA* for an Eurasian deforestation experiment.

Independently of the scenario, the trajectory densities at -96 hours have their maxima around the Baffin Island. However, the density of weak CAO trajectories ($0 \leq \Delta\theta \leq 8\text{K}$, Fig. 5e, f) in both scenarios is discernibly lower there than the density of strong CAO trajectories ($\Delta\theta > 8\text{K}$, Fig. 5g, h). The weak CAO trajectories are instead spread over a wider area, notably also more towards the east. Moreover, strong CAO trajectories more often come from more poleward regions (150°W) than
455 weak ones. Overall, there is no considerable scenario dependency of the source regions of the coldest air masses arriving at



the Labrador Sea. This implies that forest cover changes do not fundamentally change the circulation patterns associated with CAOs.

At starting time (-0 hours), trajectories of both weak and strong CAOs show smaller potential temperature differences between the atmosphere and the ocean in *forestNA* than the ones in *grassNA* (Fig. 6a). In agreement with this, CAO trajectories in *forestNA* also see weaker ocean-to-atmosphere heat fluxes (Fig. 6b) as already shown in Sect. 3.2 (Fig. 4c). Note that the probability density of weak CAOs shows several trajectories with $\Delta\theta_{tra} > 8$ K (Fig. 6a). This comes from the starting height being 100 hPa above the ground (which in the median is around 905 hPa) and not at 850 hPa (which was used for defining CAO masks). While one might expect that the reduced potential temperature difference in *forestNA* is due to warmer trajectory temperatures, this is not the case: Potential temperatures of both strong and weak CAO trajectories at starting time in *forestNA* are notably cooler than in *grassNA* (Fig. 6c). The sea ice and cool SST anomaly in the Labrador Sea in *forestNA* (Fig. 3a, e) causes the skin temperatures below the trajectories to be considerably cooler than in *grassNA* (Fig. 6d). Thus, to be part of a CAO, an air parcel in *forestNA* must be considerably cooler than in *grassNA*. This is the case 96 hours before the trajectories reach the target locations, with weak and strong CAO trajectories still being cooler in *forestNA* than in *grassNA* (Fig. 6e). Correspondingly, the total number of trajectories that are cold enough to meet a CAO threshold in *forestNA* is only about half of the one in *grassNA* (Tab. B1).

Moreover, potential skin temperatures at starting time in weak CAOs are very similar to the ones in strong CAOs while the trajectory temperatures differ considerably between the categories. This supports that the atmospheric variability is the more important trigger for CAOs than SST variability. One would not expect very low skin temperatures in CAOs as shown in the tails of weak CAOs (Fig. 6d), yet some weak CAO trajectories might be started over sea ice and very close to land which leads to very low values in θ_{skin} . Notably, the skin temperatures below the trajectories in the source region (Fig. 6f) are considerably colder than in the target region (Fig. 6d) because land is colder than the ocean. While the surface below strong CAO trajectories in the source regions in *forestNA* is slightly warmer than in *grassNA*, this is not the case for weak CAO trajectories (Fig. 6f). This is likely due to weak CAO trajectories also originating from regions east of the Labrador Sea, where the influence of the warming hole is strong in *forestNA* (Fig. 5e, f and Fig. 3a).

These results suggest a positive SST feedback mechanism initiated by the forest cover perturbations. In *forestNA*, a warmer atmosphere makes (strong) CAOs less likely. The ocean response to this is a cooling of Labrador Sea SSTs (Sect. 3.2) which in turn makes (strong) CAOs even less likely. In *grassNA*, the atmospheric response and direction of the feedback are simply reversed. This suggested mechanism of how forest cover changes affect the ocean circulation appears more evidently in *grassNA*, where the near-surface temperature in the source region of trajectories significantly cools in the long term response to forest cover removal (Fig. 1b). In *forestNA*, the source region of trajectories does not warm consistently but actually slightly cools over the Arctic Archipelago. We propose that this is a consequence of the feedback itself, i.e. that the SST cooling (and related sea ice processes) also cools the adjacent land regions. Regarding the argument that this SST feedback is initiated by warming due to forestation, it is unfortunately not meaningful to study the first few decades of the simulations. The cold bias at the branching point of the simulations (Sect. 2) makes interpreting temperature distribution changes highly complicated.

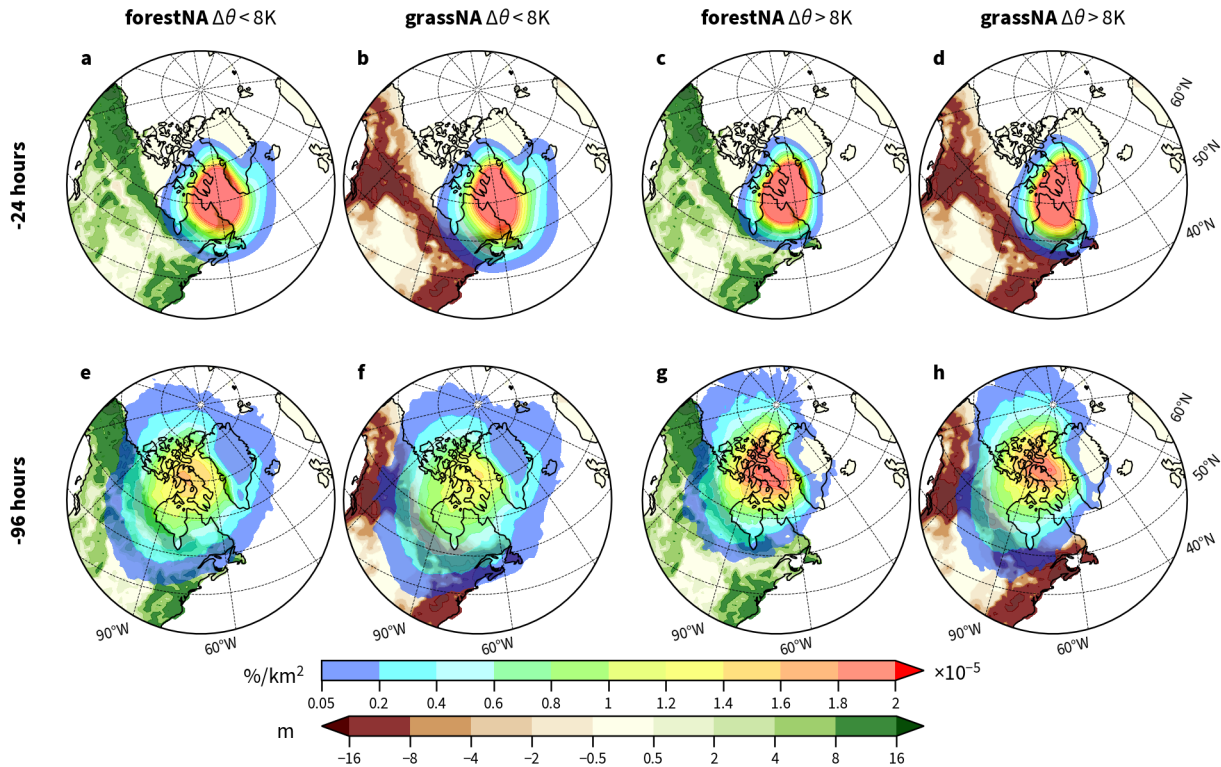


Figure 5. (a)-(d) Normalized densities of backward trajectories started in the Labrador Sea at -24 and (e)-(h) -96 hours after starting time (rainbow shading). Trajectories are grouped by the air-sea potential temperature difference $\Delta\theta$ (Sect. 2.4) at starting time into $0 \leq \Delta\theta \leq 8\text{K}$ ((a),(b),(e),(f)) and $\Delta\theta > 8\text{K}$ ((c),(d),(g),(h)). The densities are normalized as described in Sect. 2.4 and averaged for each time window over DJFMAM of years 150 to 200. Green and brown shading on land represents the average changes in canopy height in meters of the years 50 to 300.

490 To support that warming due to forestation does influence CAOs and that this initiates the SST feedback loop, we investigate the distributions of daily minimum near-surface temperatures in the source regions of the CAOs during the years 150 to 200. While the daily minimum near-surface temperature distribution over the considered source region in *forestNA* is similar to *control* (Fig. B6a), it is shifted to warmer temperatures in grid-cells with large forest cover changes (Fig. B6c). Conversely, the distributions in *grassNA* shift to lower temperatures independently of which regions are considered (Fig. B6b, d). Thus, 495 the coolest temperatures in the source region, which are needed for the formation of strong CAOs, are significantly impacted by forest cover changes in *grassNA*. In the long-term response in *forestNA*, the effect of forestation is dampened by the cool anomaly in the Labrador Sea which, in contrast to the abrupt forest cover changes, only establishes after some decades.

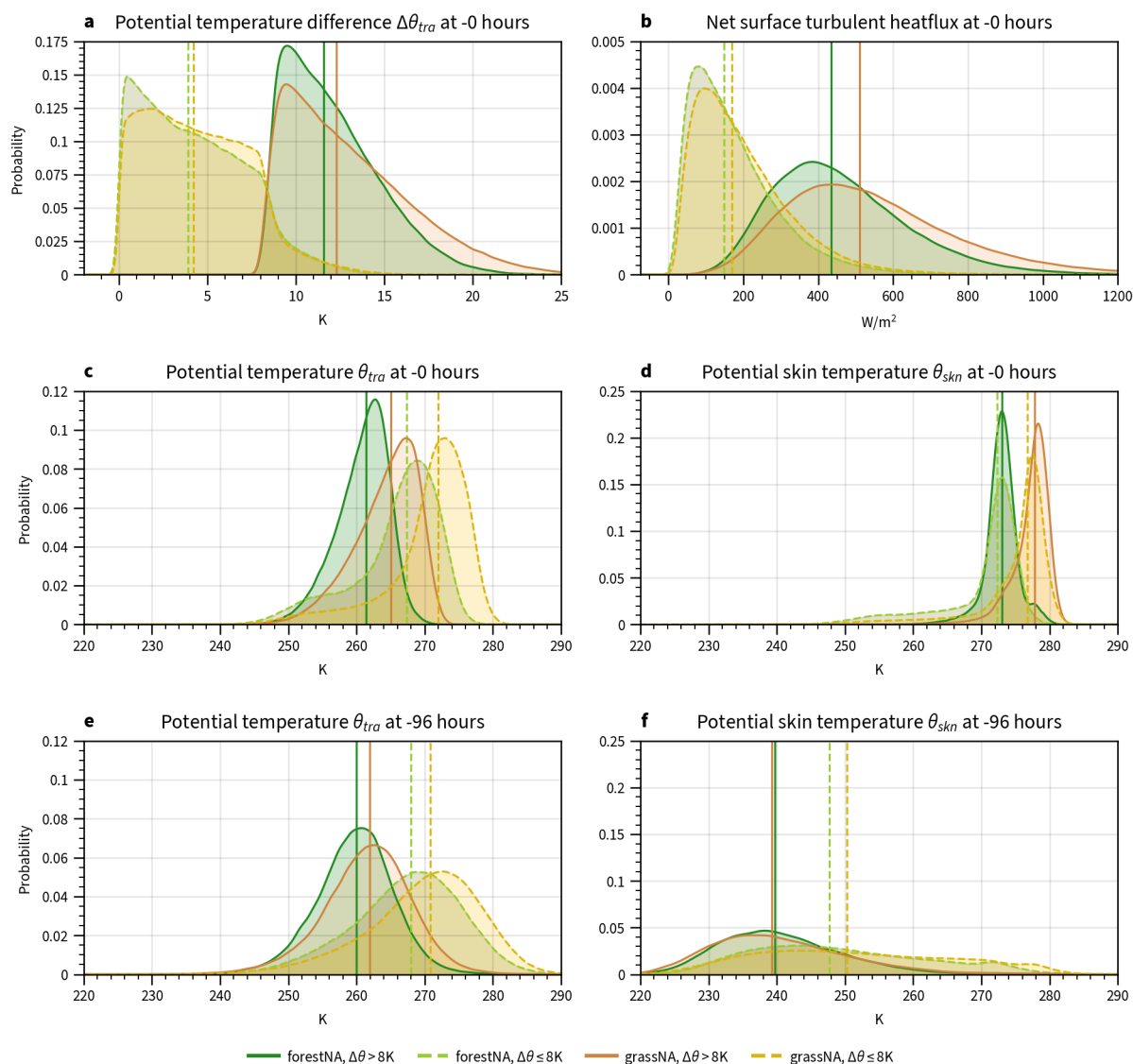


Figure 6. Probability densities of variables traced along the trajectories of (a) potential temperature difference between trajectory temperature and surface temperature at in the target region at -0 hours, (b) net turbulent heat flux below the trajectory at -0 hours, (c) potential temperature of trajectories at -0 hours, (d) potential skin temperature of the surface below the trajectories at -0 hours, (e) potential temperature of trajectories in the source region at -96 hours, and (f) potential skin temperature of the surface below the trajectories at -96 hours. Densities are estimated using kernel density estimation (Parzen, 1962) and medians are marked by vertical lines. Continuous dark lines denote strong CAO trajectories, while dashed light ones mark weak CAO trajectories, *forestNA* is depicted in green and light green while *grassNA* is brown and light brown.



3.4 Changes in wind stress forcing

In this section, we complement the previous buoyancy-focused analyses with a brief assessment of the dynamical influence of wind changes on the subpolar gyre circulation. Forest cover change goes along with a downstream surface wind response over the subpolar North Atlantic (Fig. 1c, d). The forcing of surface wind stress on the ocean circulation has been addressed in several recent studies that discuss North Atlantic surface temperature anomalies (Putrasahan et al., 2019; Hu and Fedorov, 2020; Lohmann et al., 2021; Ghosh et al., 2023), though the interplay between wind stress and buoyancy forcing (and its dependence on model resolution) on subpolar gyres is still subject of current research (Hogg and Gayen, 2020; Liu et al., 2022; Bhagtani et al., 2023). Given that wind changes have been attributed an important role in SST changes in the North Atlantic – e.g. through heat transport induced by Ekman flow (Hu and Fedorov, 2020), by shifting the North Atlantic current (Ghosh et al., 2023), or by transporting density anomalies (Kostov et al., 2024) – we want to investigate the connection between surface wind stress and North Atlantic SST anomalies in our simulations as well. We think it is insightful to inspect wind stress changes and its potential effects on the North Atlantic ocean circulation in more detail even if it is argued that decadal AMOC variability is closely related to variability of buoyancy forcing (in CESM2) as also found above (Yeager, 2015).

In an extensive analysis of the NAWH in global warming simulations, Gervais et al. (2018) find a reduction in westerlies over the North Atlantic ocean, which is qualitatively in line with reduced winds and lower North Atlantic SSTs in our *forestNA* simulation (Fig. 7a, Fig. 1a, c). In contrast, Hu and Fedorov (2020) find stronger westerlies to be associated with a more intense NAWH, which opposes our findings of not only the NAWH being linked to weaker westerlies in *forestNA*, but stronger westerlies occurring together with a cooling hole in *grassNA* (Fig. 7b, Fig. 1b). Similarly, enhanced wind stress in Lohmann et al. (2021) was linked to a strengthened gyre circulation leading to a warming hole – unlike in our *grassNA* simulation in which a stronger North Atlantic subpolar gyre is found to match a cooling hole (Fig. 7f). Note that while Lohmann et al. (2021) analyse idealized MPI runs, both Gervais et al. (2018) and Hu and Fedorov (2020) investigate CESM1 simulations. In summary, the discrepancy between Hu and Fedorov (2020) and our results suggests that arguments solely based on Ekman-induced heat transport into or out of the NAWH region are too simple.

To assess the contribution of changes in the wind-driven ocean circulation in comparison to the overall barotropic flow, we compare the estimated Sverdrup transport (Equation 3) against the model output barotropic streamfunction. Here, annual averages are chosen over DJFMAM for comparability with aforementioned studies. In *forestNA*, the anti-cyclonic wind stress curl anomaly around Greenland (Fig. 7a) induces a reduced anticyclonic flow in the Labrador Sea (Fig. 7c). In *grassNA*, the response to the positive wind stress curl in the Labrador Sea likewise is a decreased streamfunction (enhanced anticyclonic gyre circulation) in this region (Fig. 7d). South of 50°N, a negative wind stress curl anomaly extends across the North Atlantic with corresponding positive change in the wind-driven streamfunction.

For both *forestNA* and *grassNA*, the induced changes in the wind-driven streamfunction (Fig. 7c, d) are however rather small compared to changes in overall barotropic streamfunction (Fig. 7e, f). The barotropic gyre circulation is weaker (less cyclonic) in *forestNA* across the entire North Atlantic and especially at its southern flank, which results in a reduced meridional extent of the flow. However, note that the sign of the streamfunction changes agree north of 45°N which means that wind changes



potentially amplify the density-driven circulation changes. The gyre becomes stronger in *grassNA* and extends much further south than in *control*. Here, the streamfunction changes feature the same sign in the Labrador Sea and south of 40°N but the latitude of the sign flip differs by 10°. Given that the estimated changes in the wind-driven streamfunction are overall small compared to the overall barotropic streamfunction anomalies, we conclude that the gyre circulation changes can be largely attributed to density changes as other studies found before (Liu et al., 2019). How winds transport density anomalies in the gyre region (and thereby amplifying or dampening the ocean circulation response) in more detail (Kostov et al., 2024) is beyond the scope of this study.

The changes in surface wind patterns over the ocean are not uniform across the subpolar North Atlantic but contain patterns that overlap with SST changes (compare Fig. 3a,b to Fig. 7a,b around 45°N and between 50°W and 30°W). This suggests that the wind response and subsequently the effect on the ocean circulation are part of a feedback loop rather than solely a direct response to the forest cover changes upstream. In *grassNA*, for instance, an increased baroclinicity around 50°N and 40°W might be linked to an enhanced cyclone frequency that footprints in a cyclonic surface wind field anomaly seen around 43°N and 40°W (Gervais et al., 2019). The corresponding positive wind-driven streamfunction aligns with the positive change of the barotropic streamfunction, thus the induced wind pattern would act as a positive feedback in this case. Similarly in *forestNA*, the colder SSTs in the Labrador Sea correspond to a local reduction of baroclinicity, reduced cyclonic winds, and ultimately a reduction of the ocean streamfunctions. In general, however, the overall role of wind in the process chain remains difficult to identify.

Any potential SST-wind feedback loop is likely broken in Lohmann et al. (2021) due to adding a wind stress value from a separate control simulation at each grid-cell. This, in addition to other model dependencies, could explain a part of the fundamentally different simulated gyre responses between their and our study. Ruling out model dependency, the different response in Hu and Fedorov (2020) could be explained by the different model resolution (4° in Hu and Fedorov (2020) versus 1° in our simulations). Other than that, the opposing results could mean that either buoyancy forcing is the more important driver of North Atlantic ocean circulation changes (in CESM) or that the gyre circulation is very sensitive to the exact geographical distribution of wind stress changes.

4 Discussion and Conclusions

This study illustrates the biogeophysical effects of idealised North American forest cover changes on the North Atlantic ocean circulation. Foresting North America induces warming on the global scale, most pronounced over North American land itself, however with a cooling anomaly in the subpolar North Atlantic. This is known as the NAWH from other forestation but also global warming experiments (Portmann et al., 2022; Guo et al., 2024; Keil et al., 2020; Gervais et al., 2018). This cold anomaly extends downstream across Europe and Asia with local cooling in these remote regions reaching up to -1 K. Conversely, forcing North American vegetation-sustaining areas to be grasslands, global surface temperatures reduce, albeit again featuring an anomaly of opposite sign in the North Atlantic. Apart from the NAWH being of comparable magnitude, these changes are generally in line with being weaker than the global-scale equivalents (Portmann et al., 2022). The location and spatial extent

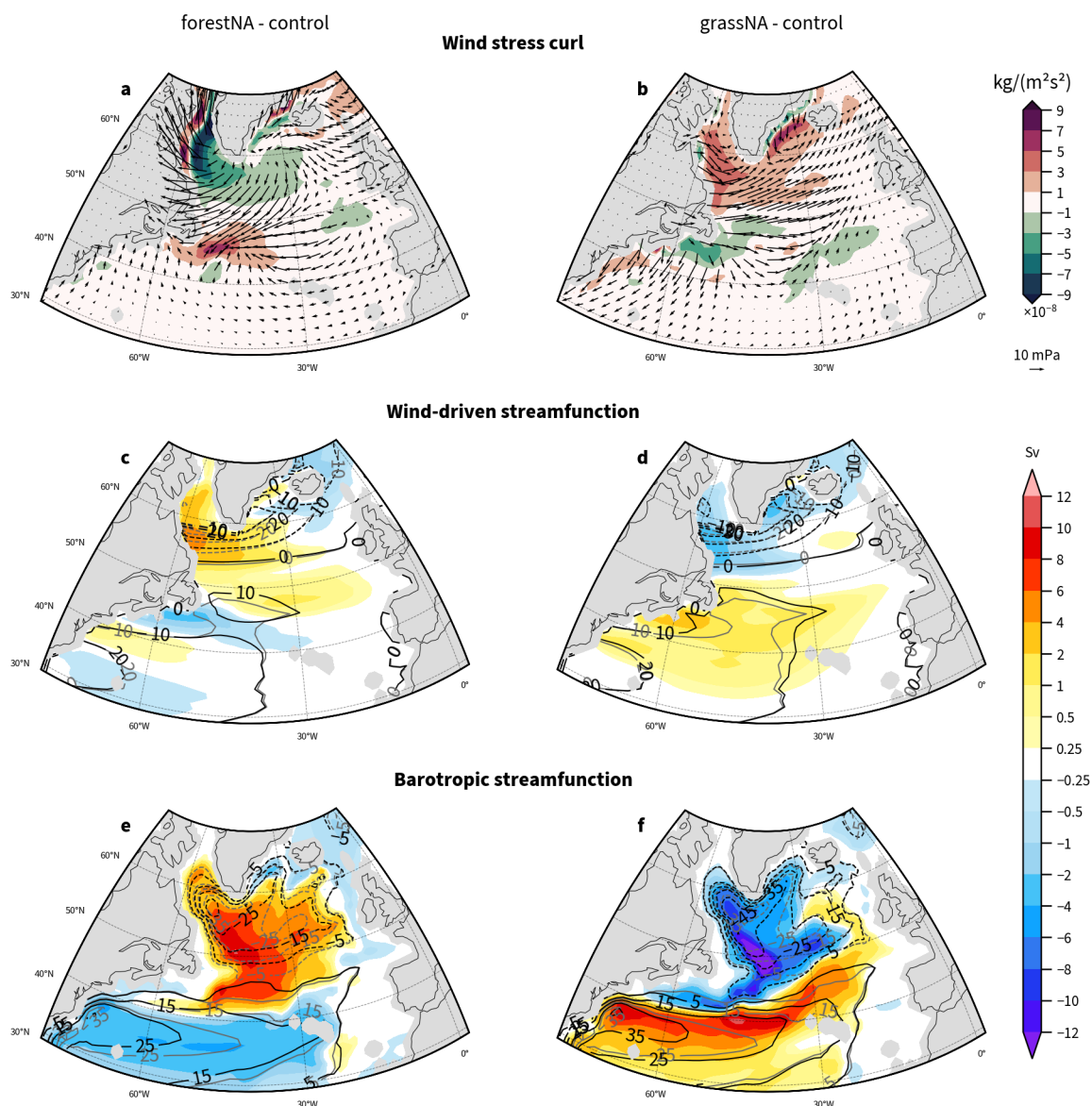


Figure 7. Annually averaged wind curl anomalies from *control* in shading with wind stress anomalies as quivers for (a) *forestNA* and (b) *grassNA*. A positive wind stress curl anomaly represents a more cyclonic curl. (c), (d) Estimated wind-driven streamfunctions of *control* (grey contours), the scenarios (black contours), and the respective anomalies of both scenarios (shading). (e), (f) The absolute barotropic streamfunction of *control* (grey contours) and the scenarios (black contours) and anomalies (shading). In (c)-(f), a negative streamfunction corresponds to a cyclonic circulation and a negative anomaly in these regions to an intensification of the flow. Data are taken again from years 50 to 300.



565 of the SST anomalies are similar to global simulations for both experiments. Thus, our findings suggest a high sensitivity of
the North Atlantic to upstream land cover changes. The changes in SSTs are accompanied by AMOC weakening in *forestNA*
and strengthening in *grassNA*. Yet, the SST response does not depend linearly on AMOC strength confirming findings by Keil
et al. (2020).

Forests directly influence (surface) wind patterns and atmospheric temperatures which in turn – in addition to freshwater
570 fluxes – drive the North Atlantic ocean circulation. In these simulations, ocean-to-atmosphere turbulent heat fluxes were identi-
fied as the leading mechanism determining the (long-term) ocean response. The related buoyancy fluxes dominate the response
over other buoyancy flux terms (Fig. 3g, h, k, l and Fig. B4). In particular, freshwater fluxes are non-negligible but only make up
for a subordinate contribution. Hereby, the extraction of heat from the ocean and thus DWF is mainly governed by strong CAOs
(Fig. 4). The frequency of CAOs decreases in *forestNA* and increases in *grassNA* (Fig. 3m, n) and so do the corresponding net
575 turbulent heat fluxes (Fig. 4). Moreover, we find that the salinity-advection feedback is likely intensifying AMOC changes but
is not the leading cause, as it is in freshwater forced simulations used to produce large changes in AMOC (van Westen et al.,
2024; van Westen and Dijkstra, 2024). It is also likely that salinity plays a role in the sensitivity of the North Atlantic ocean to
atmospheric forcing, but this mechanism needs further investigation. In addition, (de-)forestation-induced wind stress changes
are not large enough to be accountable for the gyre circulation changes (Lohmann et al., 2021; Liu et al., 2019). Comparing
580 the results with other studies featuring NAWH-like SST anomalies shows that the role of wind stress on the NAWH is more
complicated than simple Ekman transport arguments can explain.

To bridge the gap between the effect of land cover changes on the atmosphere and the effect of the atmosphere on the ocean,
we performed Lagrangian air parcel analyses. Backward trajectories from CAOs in the Labrador Sea show that the source
regions (i.e. the average synoptic situation) do not fundamentally differ between *forestNA* and *grassNA*. The upstream source
585 regions are not necessarily regions with highest forest cover changes but in general the very high latitudes. This suggests that
forest cover changes affect Arctic temperatures which contribute to making CAOs in *forestNA* less frequent and more frequent
in *grassNA* (Fig. 3m, n). This is supported by previous research of Eurasian forest cover experiments which also show similar
warming and cooling hole behaviour in (Guo et al., 2024). In *grassNA*, this mechanism appears straightforward. Deforestation
leads to a consistent cooling of daily mean and minimum temperatures in the source region (Fig. 3b and Fig. B6b). This
590 cooling results in a larger potential temperature difference with the ocean skin temperature, i.e. more CAOs and larger heat
fluxes (Fig. 6a, b). In *forestNA*, the cool anomaly in the Labrador Sea is so strong that air parcels also need to be much cooler
to induce a CAO over these colder skin temperatures (Fig. 6c d). This is a positive feedback in which an initially warmer
atmosphere makes CAOs less likely, cooling the ocean via the impacts on the ocean circulation, further making CAOs less
likely. The resulting cooling in *forestNA* is so strong that it even cools some of the trajectory source regions (Fig. 1 and
595 Fig. B6a, c), but not enough to increase CAO frequencies (Fig. 3m) or ocean-to-atmosphere heat fluxes (Fig. 3i and Fig. 6b).
Overall, the key mechanism controlling changes in heat loss from the ocean in the Labrador Sea is the change in CAO frequency
due to atmospheric temperature changes, which is a direct consequence of forest cover changes.

The cold anomaly in the Labrador Sea in *forestNA* is so strong because sea ice growth acts as a positive feedback by
insulating the ocean from heat loss. This growth of sea ice is the reason for the fact that the NAWH in *forestNA* has its greatest



600 intensity in the Labrador Sea, while this is not the case in observations and future climate simulations (Rahmstorf et al., 2015; He et al., 2022; Gervais et al., 2018). Instead, the location and extent of the warming hole in these studies is similar to the one of the warm anomaly in *grassNA*, where there is no such strong anomalous sea ice response. In addition, the strong sea ice response makes the NAWH in *forestNA* of similar strength as in global forestation experiments (Portmann et al., 2022). The ocean surface simply cannot cool much more than this. Thus, sea ice plays a pivotal role in the response of the North
605 Atlantic ocean to atmospheric forcing. Notably, the overlapping seasonality of vegetation and MLD sensitivity likely favors a large response to forest cover changes. The high latitude albedo changes are largest in winter and spring (Fig. B3) as is the positive ocean-atmosphere temperature difference. In conclusion, the North Atlantic ocean reacts very sensitively and highly non-linear to upstream forest cover changes.

This analysis is unique in using 1° spatial and 6-hourly temporal resolution fully-coupled Earth system model output for
610 analysing the North Atlantic ocean response to North American forest cover changes, including atmospheric Lagrangian backwards trajectories. The main limitation of this study is however that only one Earth system model is used. Previous research has shown that the response to vegetation changes varies strongly between different models (De Hertog et al., 2023; Boysen et al., 2020; Davin et al., 2020). Moreover, CESM was shown to model more DWF in the Labrador Sea than other models and consequently react more sensitively to atmospheric forcing in this region (Gervais et al., 2018; Hansen et al., 1999; Liu et al., 2019; Kim et al., 2024). In addition to the model itself, the ocean response also depends on the model resolution (Garcia-Quintana et al., 2019; Jackson et al., 2020; Oldenburg et al., 2022). Future research should incorporate several models including ensemble simulations for different branching points to exclude dependency of the response on the initial state of the model. Other than that, a methodological enhancement could be linking events of high vertical mixing to surface heat loss, which would require (sub-)daily surface flux data of the ocean model (to properly account for the insulation effect of sea ice).
615 This could expand on the knowledge about how much the atmosphere contributes to buoyancy changes, for instance depending on model resolution (Garcia-Quintana et al., 2019), and the relevance compared to melt-water fluxes. The analyses could also be extended to other ocean regions, as for example the Irminger Sea to study the effects of Greenland Tip Jets (Pickart et al., 2003).

Lastly, we want to point out that the setup of our simulations is idealised as it features unrealistically extreme forest cover
625 changes for the sake of identifying the mechanisms controlling the response to land cover changes in the climate system. Further research is needed to learn about reactions of the ocean and atmosphere circulation to more realistic forest cover changes, as for example in Mo et al. (2023), and how the biogeophysical effects interact with biogeochemical ones, similar to Bala et al. (2007). Simulations from several models, which possibly include different green house gas forcings, would yield more insight into the governing mechanisms in other setups. Our results suggest that land cover changes upstream of the North
630 Atlantic ocean can have a great impact on the global climate and should be managed carefully in the future. Reducing carbon emission and halting tropical deforestation are widely accepted as primary goals for decision makers, while land management can be a powerful local climate change mitigation strategy but has to take remote effects into account (Jayakrishnan and Bala, 2023).



635 *Code and data availability.* CESM is an open-source model which can be freely downloaded here (<https://www.cesm.ucar.edu/models/cesm2>, last access: 5 July 2024). The scripts used for generating and analyzing the data used in this manuscript can be found on Zenodo ([here](#)). The generated and aggregated data used in the figures as well as the full simulation data were stored at the Institute of Atmospheric and Climate Science, ETH Zurich, for at least 10 years and are available on request.

Appendix A: Computation of individual buoyancy flux components

A1 Computation of individual buoyancy flux components

640 The following are the equations used to compute the individual buoyancy flux components following Gill (1982)

$$B^{\text{rad}} = \frac{\alpha}{c_p} \cdot (SHF_QSW + LWDN_F + LWUP_F) \quad (\text{A1})$$

$$B^{\text{turb}} = \frac{\alpha}{c_p} \cdot (SENH_F + L_v \rho_F \cdot EVAP_F) \quad (\text{A2})$$

$$B^{\text{PERO}} = \beta \rho_S S \cdot (PREC_F + EVAP_F + ROFF_F) \quad (\text{A3})$$

$$B^{\text{ICE}_{FW}} = \beta \rho_S S \cdot (IOFF_F + MELT_F) \quad (\text{A4})$$

645
$$B^{\text{melt}_H} = \frac{\alpha}{c_p} \cdot (QFLUX + MELTH_F) - \frac{\alpha L_f \rho_F}{c_p} \cdot (IOFF_F - SNOW_F) \quad (\text{A5})$$

with α the thermal expansion coefficient, β the haline contraction coefficient and other abbreviations of the model variables as found in Table A1.



	Abbreviation	Description	Value (if constant in the model)
water fluxes F_{FW}	PREC_F	Precipitation Flux from Coupler (rain+snow)	
	EVAP_F	Evaporation Flux from Coupler	
	MELT_F	Melt Flux from Coupler	
	ROFF_F	Runoff Flux from Coupler	
	IOFF_F	Ice Runoff Flux from Coupler due to Land-Model Snow Capping	
	SNOW_F	Snow Flux from Coupler	
heat fluxes Q	SHF_QSW	Solar Short-Wave Heat Flux (dn)	
	LWDN_F	Longwave Heat Flux (dn) from Coupler	
	LWUP_F	Longwave Heat Flux (up) from Coupler	
	SENH_F	Sensible Heat Flux from Coupler	
	MELTH_F	Melt Heat Flux from Coupler	
	QFLUX	Internal Ocean Heat Flux Due to Ice Formation	
constants	c_p	specific heat content of water	$4 \times 10^3 \text{ J kg}^{-1} \text{ K}^{-1}$
	L_v	latent heat of fusion	$3.337 \times 10^5 \text{ J kg}^{-1}$
	L_F	latent heat of vaporization	$2.501 \times 10^5 \text{ J kg}^{-1}$
	ρ_F	density of fresh water	$1 \times 10^3 \text{ kg m}^3$
	ρ_S	density of salt water	$1.026 \times 10^3 \text{ kg m}^3$

Table A1. List of CESM output variables used for the buoyancy flux decomposition. Water fluxes are given in $\text{kg m}^{-2} \text{ s}^{-1}$ and heat fluxes in W m^{-2} .

Appendix B: Additional material

<i>forestNA</i> $\Delta\theta \leq 8 \text{ K}$	<i>grassNA</i> $\Delta\theta \leq 8 \text{ K}$	<i>forestNA</i> $\Delta\theta > 8 \text{ K}$	<i>grassNA</i> $\Delta\theta > 8 \text{ K}$
0.167500×10^6	0.729875×10^6	0.477762×10^6	1.257228×10^6

Table B1. Absolute number of backwards trajectories started in the Labrador Sea from year 150 to 200 in DJFMAM.

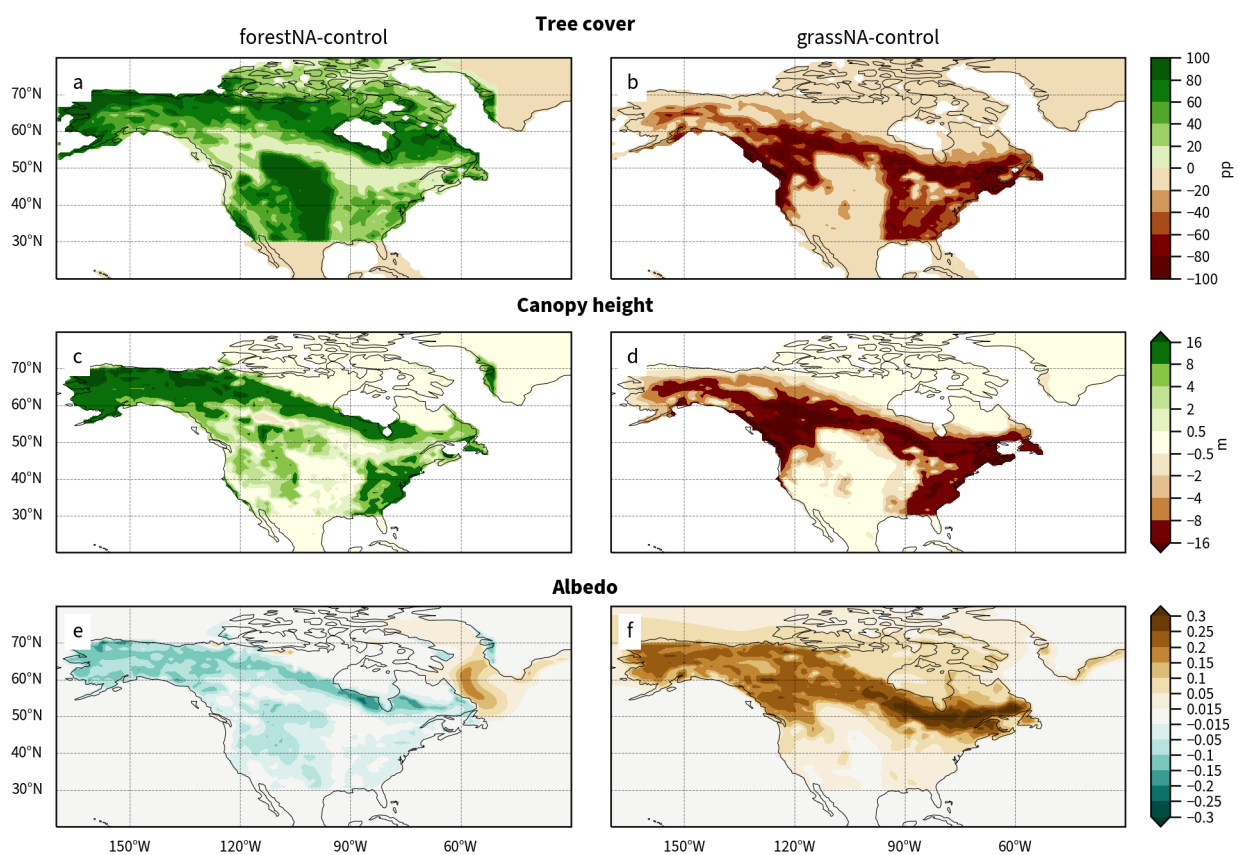


Figure B1. (a), (b) Changes of forest cover in percent point (pp), (c), (d) yearly average changes in top canopy height in meter from years 50 to 300, (e) & (f) yearly average changes in surface Albedo from years 50 to 300 for *forestNA* (left) and *grassNA* (right) compared to *control*.

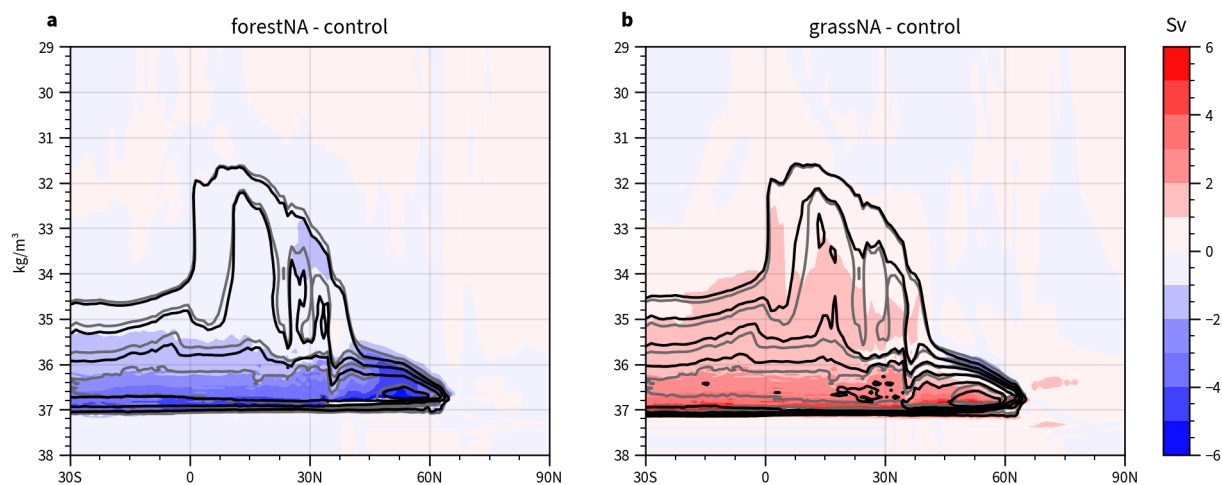


Figure B2. Changes in AMOC in potential density coordinates (a) between *forestNA* and *control* and (b) between *grassNA* and *control* (shading). As in Fig. 2, black contours denote the absolute values of the corresponding perturbation scenario while grey contours refer to *control*.

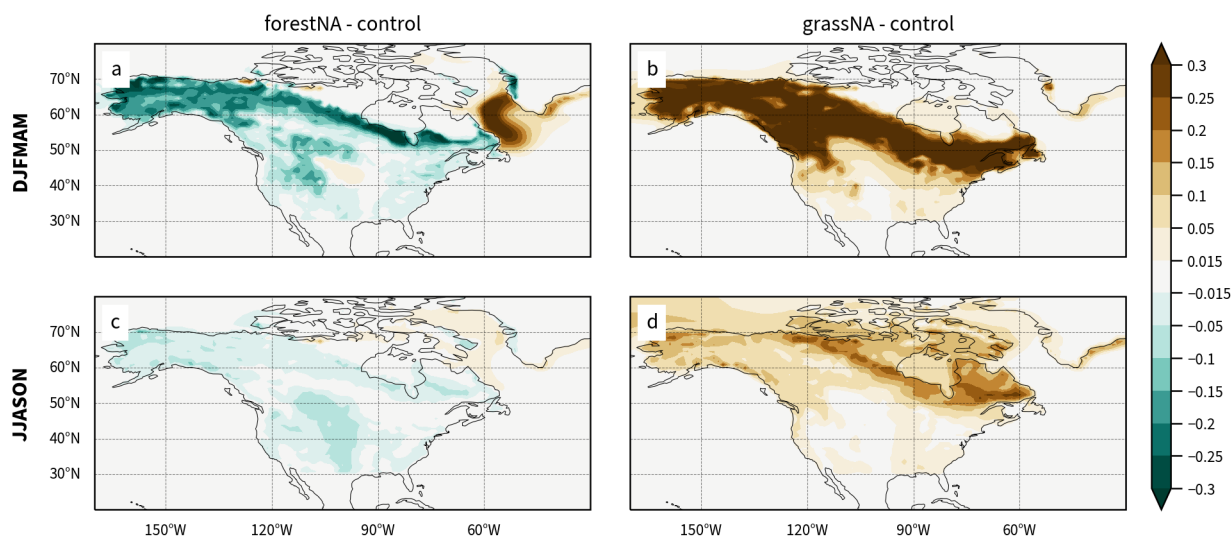


Figure B3. Map of seasonal average surface albedo response from years 50 to 300 for *forestNA* (left) and *grassNA* (right) for (a), (b) DJFMAM and (c), (d) JJASON.

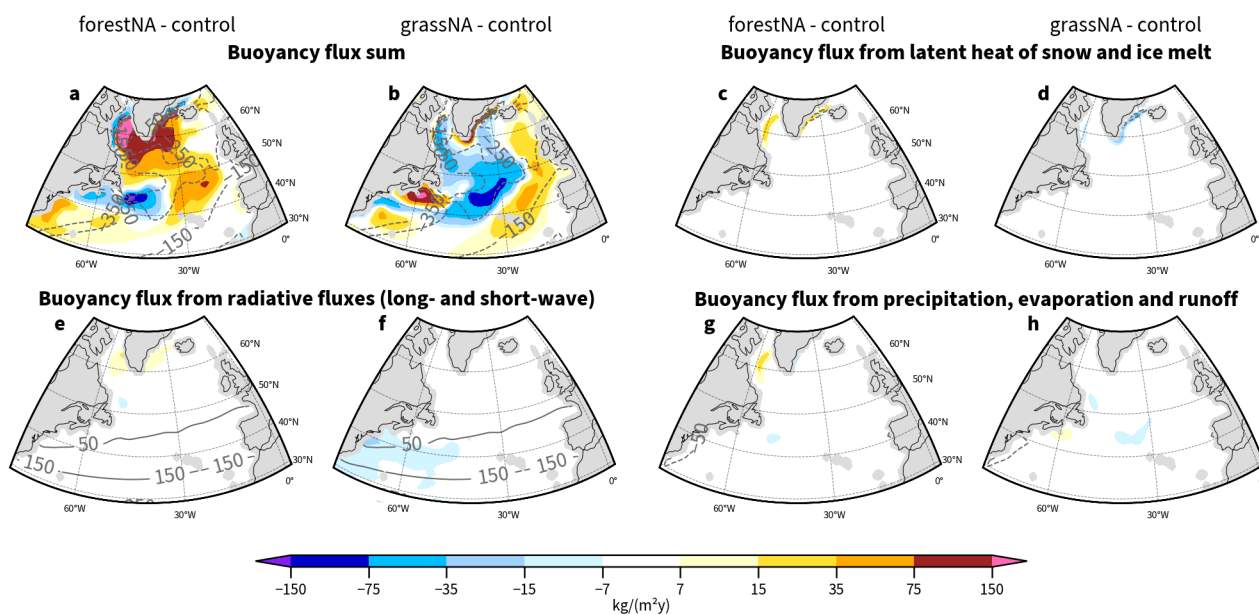


Figure B4. Remaining buoyancy flux components not shown in the main text during DJFMAM: (a), (b) sum of all buoyancy flux terms B , (c), (d) melt heat buoyancy fluxes B^{melt_H} , (e), (f) radiation-related buoyancy fluxes B^{rad} , (g), (h) and precipitation, evaporation, and runoff buoyancy fluxes B^{PERO} . Note the non-linear color shading.

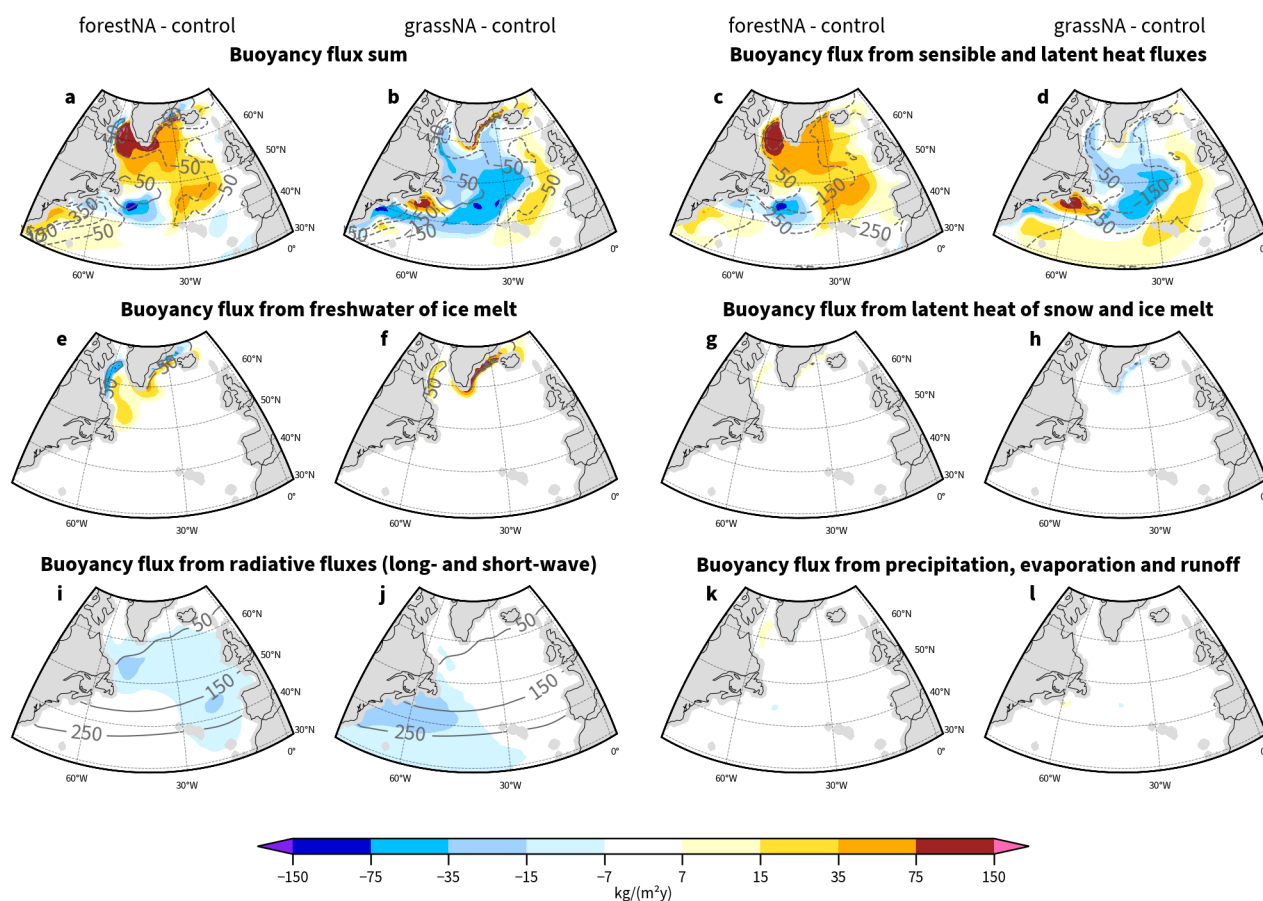


Figure B5. Differences of yearly averaged buoyancy fluxes between *forestNA* and *control* and *grassNA* and *control*, respectively: (a), (b) sum of all buoyancy flux terms B , (c), (d) buoyancy fluxes associated with turbulent heat fluxes B^{turb} , (e), (f) melt-water buoyancy fluxes B^{ICEFW} , (g), (h) melt heat buoyancy fluxes B^{melt_H} , (i), (j) radiation-related buoyancy fluxes B^{rad} , and (k), (l) precipitation, evaporation, and runoff buoyancy fluxes. Grey contours show *control* values. Note the non-linear color shading.

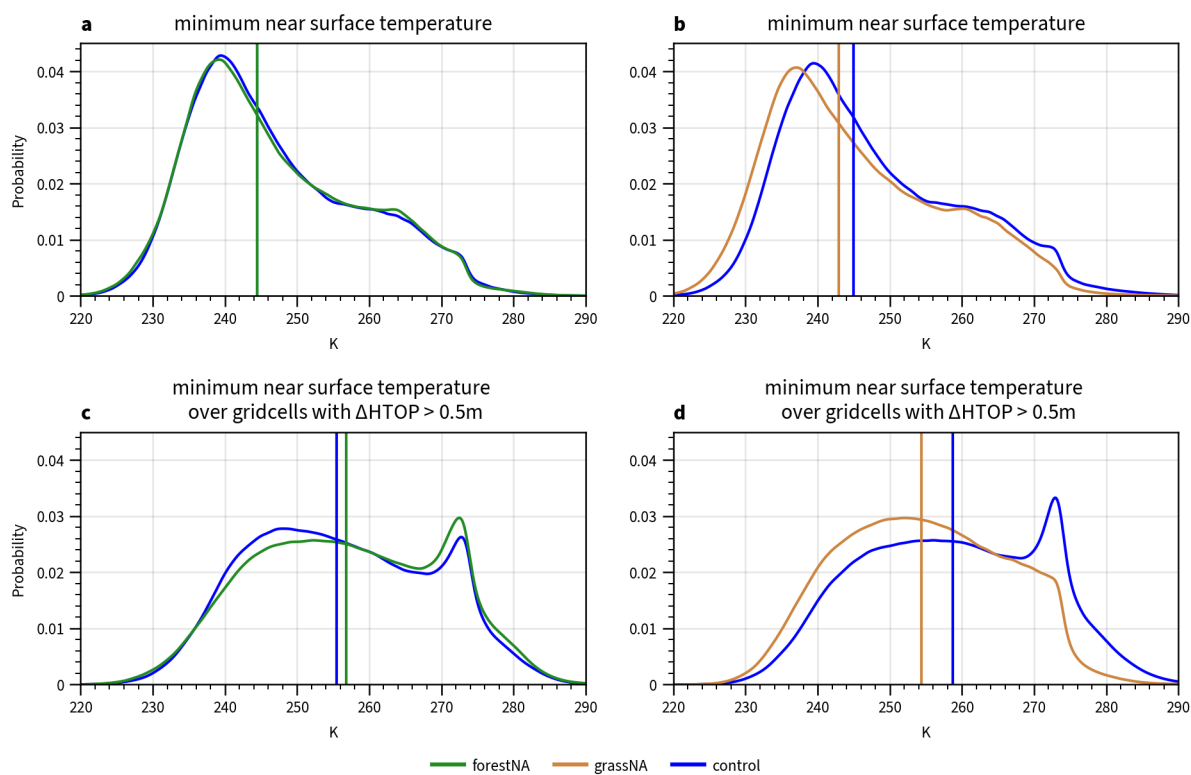


Figure B6. Probability densities of daily minimum near-surface temperature of grid-cells masked with trajectory densities $>0.05 \times 10^{-5} \% \text{m}^{-2}$ for DJFMAM in the years 150 to 200 for (a) *forestNA* (green), (b) *grassNA* (brown), and only including grid-cells with changes in canopy height $>0.5\text{m}$ for (c) *forestNA*, and (d) *grassNA* in comparison to *control* (blue). Probabilities are estimated using kernel density estimation (Parzen, 1962).



Author contributions. Conceptualization: S.S., R.P., J.Zi.; methodology: S.J.DH., S.S., R.P.; formal analysis and investigation: V.M.B., J.Zi.,
650 J.Zh.; writing/original draft preparation: V.M.B., J.Zi., J.Zh.; editing: S.S., R.P., S.J.DH., J.Zh., G.K.E., J.Zi.; visualization: V.M.B., J.Zi.;
supervision: S.S., R.P., G.K.E., J.Zi.; project administration: S.S. All authors have read and agreed to the published version of the manuscript.

Competing interests. The contact author declares that none of the authors have any competing interests.

Acknowledgements. We thank Urs Beyerle for setting up the simulations and technical support during data analysis. Moreover, we are
grateful for valuable discussions with colleagues and feedback on draft versions of this text, in particular Anna Merrifield, Felix Jäger, Joas
655 Müller, Mona Bukenberger, and Dana Grund.



References

- Armstrong McKay, D. I., Staal, A., Abrams, J. F., Winkelmann, R., Sakschewski, B., Loriani, S., Fetzer, I., Cornell, S. E., Rockström, J., and Lenton, T. M.: Exceeding 1.5°C global warming could trigger multiple climate tipping points, *Science*, 377, <https://doi.org/10.1126/science.abn7950>, 2022.
- 660 Asselin, O., Leduc, M., Paquin, D., Di Luca, A., Winger, K., Bukovsky, M., Music, B., and Giguère, M.: On the Intercontinental Transferability of Regional Climate Model Response to Severe Forestation, *Climate 2022*, Vol. 10, Page 138, 10, 138, <https://doi.org/10.3390/CLI10100138>, 2022.
- Bala, G., Caldeira, K., Wickett, M., Phillips, T. J., Lobell, D. B., Delire, C., and Mirin, A.: Combined climate and carbon-cycle effects of large-scale deforestation, *Proceedings of the National Academy of Sciences of the United States of America*, 104, 6550–6555, 665 <https://doi.org/10.1073/PNAS.0608998104>, 2007.
- Bastin, J. F., Finegold, Y., Garcia, C., Mollicone, D., Rezende, M., Routh, D., Zohner, C. M., and Crowther, T. W.: The global tree restoration potential, *Science*, 364, 76–79, https://doi.org/10.1126/SCIENCE.AAX0848/SUPPL_FILE/AAX0848_BASTIN_SM_DATA-FILE-S2.CSV, 2019.
- Betts, R. A.: Offset of the potential carbon sink from boreal forestation by decreases in surface albedo, *Nature*, 408, 187–190, 670 <https://doi.org/10.1038/35041545>, 2000.
- Bhagtani, D., Hogg, A. M., Holmes, R. M., and Constantinou, N. C.: Surface Heating Steers Planetary-Scale Ocean Circulation, *Journal of Physical Oceanography*, 53, 2375–2391, <https://doi.org/10.1175/JPO-D-23-0016.1>, 2023.
- Bonan, G. B.: Forests and climate change: Forcings, feedbacks, and the climate benefits of forests, *Science*, 320, 1444–1449, <https://doi.org/10.1126/SCIENCE.1155121>, 2008.
- 675 Böning, C. W., Wagner, P., Handmann, P., Schwarzkopf, F. U., Getzlaff, K., and Biastoch, A.: Decadal changes in Atlantic overturning due to the excessive 1990s Labrador Sea convection, *Nature Communications* 2023 14:1, 14, 1–10, <https://doi.org/10.1038/s41467-023-40323-9>, 2023.
- Born, A., Stocker, T. F., and Sandø, A. B.: Transport of salt and freshwater in the Atlantic Subpolar Gyre, *Ocean Dynamics*, 66, 1051–1064, <https://doi.org/10.1007/s10236-016-0970-y>, 2016.
- 680 Boysen, L. R., Brovkin, V., Pongratz, J., Lawrence, D. M., Lawrence, P., Vuichard, N., Peylin, P., Liddicoat, S., Hajima, T., Zhang, Y., Rocher, M., Delire, C., Séférian, R., Arora, V. K., Nieradzik, L., Anthoni, P., Thiery, W., Laguë, M. M., Lawrence, D., and Lo, M.-H.: Global climate response to idealized deforestation in CMIP6 models, *Biogeosciences*, 17, 5615–5638, <https://doi.org/10.5194/bg-17-5615-2020>, 2020.
- Caesar, L., Rahmstorf, S., Robinson, A., Feulner, G., and Saba, V.: Observed fingerprint of a weakening Atlantic Ocean overturning circulation, *Nature* 2018 556:7700, 556, 191–196, <https://doi.org/10.1038/s41586-018-0006-5>, 2018.
- Chen, G., Huang, R. X., Peng, Q., and Chu, X.: A Time-Dependent Sverdrup Relation and Its Application to the Indian Ocean, *Journal of Physical Oceanography*, 52, 1233–1244, <https://doi.org/10.1175/JPO-D-21-0223.1>, 2022.
- Danabasoglu, G., Lamarque, J. F., Bacmeister, J., Bailey, D. A., DuVivier, A. K., Edwards, J., Emmons, L. K., Fasullo, J., Garcia, R., Gettelman, A., Hannay, C., Holland, M. M., Large, W. G., Lauritzen, P. H., Lawrence, D. M., Lenaerts, J. T., Lindsay, K., Lipscomb, 690 W. H., Mills, M. J., Neale, R., Oleson, K. W., Otto-Bliesner, B., Phillips, A. S., Sacks, W., Tilmes, S., van Kampenhout, L., Vertenstein, M., Bertini, A., Dennis, J., Deser, C., Fischer, C., Fox-Kemper, B., Kay, J. E., Kinnison, D., Kushner, P. J., Larson, V. E., Long, M. C.,



- Mickelson, S., Moore, J. K., Nienhouse, E., Polvani, L., Rasch, P. J., and Strand, W. G.: The Community Earth System Model Version 2 (CESM2), *Journal of Advances in Modeling Earth Systems*, 12, e2019MS001916, <https://doi.org/10.1029/2019MS001916>, 2020.
- 695 Davin, E. L. and de Noblet-Ducoudre, N.: Climatic Impact of Global-Scale Deforestation: Radiative versus Nonradiative Processes, *Journal of Climate*, 23, 97–112, <https://doi.org/10.1175/2009JCLI3102.1>, 2010.
- Davin, E. L., Rechid, D., Breil, M., Cardoso, R. M., Coppola, E., Hoffmann, P., Jach, L. L., Katragkou, E., De Noblet-Ducoudré, N., Radtke, K., Raffa, M., Soares, P. M., Sofiadis, G., Strada, S., Strandberg, G., Tölle, M. H., Warrach-Sagi, K., and Wulfmeyer, V.: Biogeophysical impacts of forestation in Europe: First results from the LUCAS (Land Use and Climate across Scales) regional climate model intercomparison, *Earth System Dynamics*, 11, 183–200, <https://doi.org/10.5194/ESD-11-183-2020>, 2020.
- 700 De Hertog, S. J., Havermann, F., Vanderkelen, I., Guo, S., Luo, F., Manola, I., Coumou, D., Davin, E. L., Duveiller, G., Lejeune, Q., Pongratz, J., Schleussner, C.-F., Seneviratne, S. I., and Thiery, W.: The biogeophysical effects of idealized land cover and land management changes in Earth system models, *Earth System Dynamics*, 14, 629–667, <https://doi.org/10.5194/esd-14-629-2023>, 2023.
- De Hertog, S. J., Lopez-Fabara, C. E., van der Ent, R., Keune, J., Miralles, D. G., Portmann, R., Schemm, S., Havermann, F., Guo, S., Luo, F., Manola, I., Lejeune, Q., Pongratz, J., Schleussner, C.-F., Seneviratne, S. I., and Thiery, W.: Effects of idealized land cover and land management changes on the atmospheric water cycle, *Earth System Dynamics*, 15, 265–291, <https://doi.org/10.5194/esd-15-265-2024>, 2024.
- 705 Ditlevsen, P. and Ditlevsen, S.: Warning of a forthcoming collapse of the Atlantic meridional overturning circulation, *Nature Communications*, 14, <https://doi.org/10.1038/S41467-023-39810-W>, 2023.
- Fan, Y., Lu, J., and Li, L.: Mechanism of the Centennial Subpolar North Atlantic Cooling Trend in the FGOALS-g2 Historical Simulation, *Journal of Geophysical Research: Oceans*, 126, <https://doi.org/10.1029/2021JC017511>, 2021.
- 710 Garcia-Quintana, Y., Courtois, P., Hu, X., Pennelly, C., Kieke, D., and Myers, P. G.: Sensitivity of Labrador Sea Water Formation to Changes in Model Resolution, Atmospheric Forcing, and Freshwater Input, *Journal of Geophysical Research: Oceans*, 124, 2126–2152, <https://doi.org/10.1029/2018JC014459>, 2019.
- Gelderloos, R., Straneo, F., and Katsman, C. A.: Mechanisms behind the Temporary Shutdown of Deep Convection in the Labrador Sea: Lessons from the Great Salinity Anomaly Years 1968–71, *Journal of Climate*, 25, 6743–6755, <https://doi.org/10.1175/JCLI-D-11-00549.1>, 2012.
- 715 Gervais, M., Shaman, J., and Kushnir, Y.: Mechanisms Governing the Development of the North Atlantic Warming Hole in the CESM-LE Future Climate Simulations, *Journal of Climate*, 31, 5927–5946, <https://doi.org/10.1175/JCLI-D-17-0635.1>, 2018.
- Gervais, M., Shaman, J., and Kushnir, Y.: Impacts of the North Atlantic Warming Hole in Future Climate Projections: Mean Atmospheric Circulation and the North Atlantic Jet, *Journal of Climate*, 32, 2673–2689, <https://doi.org/10.1175/JCLI-D-18-0647.1>, 2019.
- 720 Ghosh, R., Putrasahan, D., Manzini, E., Lohmann, K., Keil, P., Hand, R., Bader, J., Matei, D., and Jungclaus, J. H.: Two Distinct Phases of North Atlantic Eastern Subpolar Gyre and Warming Hole Evolution under Global Warming, *Journal of Climate*, 36, 1881–1894, <https://doi.org/10.1175/JCLI-D-22-0222.1>, 2023.
- Gill, A. E.: *Atmosphere-Ocean Dynamics*, vol. 30, Academic Press, Cambridge, England, ISBN 0-12-283520-4, 1982.
- 725 Griscom, B. W., Adams, J., Ellis, P. W., Houghton, R. A., Lomax, G., Miteva, D. A., Schlesinger, W. H., Shoch, D., Siikamäki, J. V., Smith, P., Woodbury, P., Zganjar, C., Blackman, A., Campari, J., Conant, R. T., Delgado, C., Elias, P., Gopalakrishna, T., Hamsik, M. R., Herrero, M., Kiesecker, J., Landis, E., Laestadius, L., Leavitt, S. M., Minnemeyer, S., Polasky, S., Potapov, P., Putz, F. E., Sanderman, J., Silvius, M., Wollenberg, E., and Fargione, J.: Natural climate solutions, *Proceedings of the National Academy of Sciences of the United States of America*, 114, 11 645–11 650, https://doi.org/10.1073/PNAS.1710465114/SUPPL_FILE/PNAS.1710465114.SAPP.PDF, 2017.



- 730 Guo, J., Liu, Y., and Hu, Y.: Climate Response to Vegetation Removal on Different Continents, *Journal of Geophysical Research: Atmospheres*, 129, e2023JD039 531, <https://doi.org/10.1029/2023JD039531>, 2024.
- Hansen, J., Ruedy, R., Glascoe, J., and Sato, M.: GISS analysis of surface temperature change, *Journal of Geophysical Research Atmospheres*, 104, 30 997–31 022, <https://doi.org/10.1029/1999JD900835>, 1999.
- He, C., Clement, A. C., Cane, M. A., Murphy, L. N., Klavans, J. M., and Fenske, T. M.: A North Atlantic Warming Hole Without Ocean
735 Circulation, *Geophysical Research Letters*, 49, <https://doi.org/10.1029/2022GL100420>, 2022.
- Henry, L. G., McManus, J. F., Curry, W. B., Roberts, N. L., Piotrowski, A. M., and Keigwin, L. D.: North Atlantic ocean circulation and abrupt climate change during the last glaciation, *Science*, 353, 470–474, <https://doi.org/10.1126/science.aaf5529>, 2016.
- Hogan, E. and Sriver, R. L.: The Effect of Internal Variability on Ocean Temperature Adjustment in a Low-Resolution CESM Initial Condition Ensemble, *Journal of Geophysical Research: Oceans*, 124, 1063–1073, <https://doi.org/10.1029/2018JC014535>, 2019.
- 740 Hogg, A. M. C. and Gayen, B.: Ocean Gyres Driven by Surface Buoyancy Forcing, *Geophysical Research Letters*, 47, e2020GL088 539, <https://doi.org/10.1029/2020GL088539>, 2020.
- Holdsworth, A. M. and Myers, P. G.: The Influence of High-Frequency Atmospheric Forcing on the Circulation and Deep Convection of the Labrador Sea, *Journal of Climate*, 28, 4980–4996, <https://doi.org/10.1175/JCLI-D-14-00564.1>, 2015.
- Hu, S. and Fedorov, A. V.: Indian Ocean warming as a driver of the North Atlantic warming hole, *Nature Communications*, 11, <https://doi.org/10.1038/s41467-020-18522-5>, 2020.
- 745 Hua, W., Zhou, L., Dai, A., Chen, H., and Liu, Y.: Important non-local effects of deforestation on cloud cover changes in CMIP6 models, *Environmental Research Letters*, 18, 094 047, <https://doi.org/10.1088/1748-9326/ACF232>, 2023.
- IOC, SCOR, and IAPSO: The international thermodynamic equation of seawater - 2010: Calculation and use of thermodynamic properties Intergovernmental Oceanographic Commission. Intergovernmental Oceanographic Commission, Manuals and Guides No. 56, Tech. rep.,
750 UNSECO (English), https://www.teos-10.org/pubs/TEOS-10_Manual.pdf, 2010.
- Jackson, L. C., Roberts, M. J., Hewitt, H. T., Iovino, D., Koenigk, T., Meccia, V. L., Roberts, C. D., Ruprich-Robert, Y., and Wood, R. A.: Impact of ocean resolution and mean state on the rate of AMOC weakening, *Climate Dynamics*, 55, 1711–1732, <https://doi.org/10.1007/s00382-020-05345-9>, 2020.
- Jayakrishnan, K. U. and Bala, G.: A comparison of the climate and carbon cycle effects of carbon removal by afforestation and an equivalent
755 reduction in fossil fuel emissions, *Biogeosciences*, 20, 1863–1877, <https://doi.org/10.5194/bg-20-1863-2023>, 2023.
- Jiao, T., Williams, C. A., Ghimire, B., Masek, J., Gao, F., and Schaaf, C.: Global climate forcing from albedo change caused by large-scale deforestation and reforestation: Quantification and attribution of geographic variation, *Climatic Change*, 142, 463–476, <https://doi.org/10.1007/s10584-017-1962-8>, 2017.
- Keil, P., Mauritsen, T., Jungclaus, J., Hedemann, C., Olonscheck, D., and Ghosh, R.: Multiple drivers of the North Atlantic warming hole,
760 *Nature Climate Change*, 10, 667–671, <https://doi.org/10.1038/s41558-020-0819-8>, 2020.
- Kim, W. M., Ruprich-Robert, Y., Zhao, A., Yeager, S., and Robson, J.: North Atlantic Response to Observed North Atlantic Oscillation Surface Heat Flux in Three Climate Models, *Journal of Climate*, 37, 1777–1796, <https://doi.org/10.1175/JCLI-D-23-0301.1>, 2024.
- Kostov, Y., Messias, M.-J., Mercier, H., Marshall, D. P., and Johnson, H. L.: Surface factors controlling the volume of accumulated Labrador Sea Water, *Ocean Science*, 20, 521–547, <https://doi.org/10.5194/OS-20-521-2024>, 2024.
- 765 Kuhlbrodt, T., Titz, S., Feudel, U., and Rahmstorf, S.: A simple model of seasonal open ocean convection - Part II: Labrador Sea stability and stochastic forcing, *Ocean Dynamics*, 52, 36–49, <https://doi.org/10.1007/s10236-001-8175-3>, 2001.



- Lenton, T. M., Held, H., Kriegler, E., Hall, J. W., Lucht, W., Rahmstorf, S., and Schellnhuber, H. J.: Tipping elements in the Earth's climate system, *Proceedings of the National Academy of Sciences*, 105, 1786–1793, <https://doi.org/10.1073/pnas.0705414105>, 2008.
- Li, Y., Zhao, M., Motesharrei, S., Mu, Q., Kalnay, E., and Li, S.: Local cooling and warming effects of forests based on satellite observations, *Nature Communications* 2015 6:1, 6, 1–8, <https://doi.org/10.1038/ncomms7603>, 2015.
- 770 Liu, T., Ou, H. W., Liu, X., Qian, Y. K., and Chen, D.: The dependence of upper ocean gyres on wind and buoyancy forcing, *Geoscience Letters*, 9, 1–8, <https://doi.org/10.1186/S40562-022-00213-2/FIGURES/4>, 2022.
- Liu, W., Fedorov, A., and Sévellec, F.: The Mechanisms of the Atlantic Meridional Overturning Circulation Slowdown Induced by Arctic Sea Ice Decline, *Journal of Climate*, 32, 977–996, <https://doi.org/10.1175/JCLI-D-18-0231.1>, 2019.
- 775 Liu, W., Fedorov, A. V., Xie, S. P., and Hu, S.: Climate impacts of a weakened Atlantic meridional overturning circulation in a warming climate, *Science Advances*, 6, <https://doi.org/10.1126/sciadv.aaz4876>, 2020.
- Lohmann, K., Putrasahan, D. A., von Storch, J. S., Gutjahr, O., Jungclaus, J. H., and Haak, H.: Response of Northern North Atlantic and Atlantic Meridional Overturning Circulation to Reduced and Enhanced Wind Stress Forcing, *Journal of Geophysical Research: Oceans*, 126, e2021JC017902, <https://doi.org/10.1029/2021JC017902>, 2021.
- 780 Luo, H., Bracco, A., and Zhang, F.: The Seasonality of Convective Events in the Labrador Sea, *Journal of Climate*, 27, 6456–6471, <https://doi.org/10.1175/JCLI-D-14-00009.1>, 2014.
- Lynch-Stieglitz, J.: The Atlantic Meridional Overturning Circulation and Abrupt Climate Change, *Annual Review of Marine Science*, 9, 83–104, <https://doi.org/10.1146/annurev-marine-010816-060415>, 2017.
- Mahmood, R., Pielke, R. A., Hubbard, K. G., Niyogi, D., Dirmeyer, P. A., Mcalpine, C., Carleton, A. M., Hale, R., Gameda, S., Beltrán-Przekurat, A., Baker, B., Mcnider, R., Legates, D. R., Shepherd, M., Du, J., Blanken, P. D., Frauenfeld, O. W., Nair, U. S., and Fall, S.: Land cover changes and their biogeophysical effects on climate, *International Journal of Climatology*, 34, 929–953, <https://doi.org/10.1002/joc.3736>, 2014.
- Martin, T., Biastoch, A., Lohmann, G., Mikolajewicz, U., and Wang, X.: On Timescales and Reversibility of the Ocean's Response to Enhanced Greenland Ice Sheet Melting in Comprehensive Climate Models, *Geophysical Research Letters*, 49, e2021GL097114, <https://doi.org/10.1029/2021GL097114>, 2022.
- 790 McDougall, T. J. and Barker, P. M.: Getting started with TEOS-10 and the Gibbs Seawater (GSW) Oceanographic Toolbox, SCOR/IAPSO WG127, ISBN 978-0-646-55621-5, 2011.
- Menary, M. B. and Wood, R. A.: An anatomy of the projected North Atlantic warming hole in CMIP5 models, *Climate Dynamics*, 50, 3063–3080, <https://doi.org/10.1007/s00382-017-3793-8>, 2018.
- 795 Mo, L., Zohner, C. M., Reich, P. B., Liang, J., de Miguel, S., Nabuurs, G.-J., Renner, S. S., van den Hoogen, J., Araza, A., Herold, M., Mirzaghali, L., Ma, H., Averill, C., Phillips, O. L., Gamarra, J. G. P., Hordijk, I., Routh, D., Abegg, M., Adou Yao, Y. C., Alberti, G., Almeyda Zambrano, A. M., Alvarado, B. V., Alvarez-Dávila, E., Alvarez-Loayza, P., Alves, L. F., Amaral, I., Ammer, C., Antón-Fernández, C., Araujo-Murakami, A., Arroyo, L., Avitabile, V., Aymard, G. A., Baker, T. R., Bałazy, R., Banki, O., Barroso, J. G., Bastian, M. L., Bastin, J.-F., Birigazzi, L., Birnbaum, P., Bitariho, R., Boeckx, P., Bongers, F., Bouriaud, O., Brancalion, P. H. S., Brandl, S., Brearley, F. Q., Brienen, R., Broadbent, E. N., Bruelheide, H., Bussotti, F., Cazzolla Gatti, R., César, R. G., Cesljar, G., Chazdon, R. L., Chen, H. Y. H., Chisholm, C., Cho, H., Cienciala, E., Clark, C., Clark, D., Colletta, G. D., Coomes, D. A., Cornejo Valverde, F., Corral-Rivas, J. J., Crim, P. M., Cumming, J. R., Dayanandan, S., de Gasper, A. L., Decuyper, M., Derroire, G., DeVries, B., Djordjevic, I., Dolezal, J., Dourdain, A., Engone Obiang, N. L., Enquist, B. J., Eyre, T. J., Fandohan, A. B., Fayle, T. M., Feldpausch, T. R., Ferreira, L. V., Finér, L., Fischer, M., Fletcher, C., Frizzera, L., Gianelle, D., Glick, H. B., Harris, D. J., Hector, A., Hemp, A., Hengeveld, G.,
- 800



- 805 Héroult, B., Herbohn, J. L., Hillers, A., Honorio Coronado, E. N., Hui, C., Ibanez, T., Imai, N., Jagodziński, A. M., Jaroszewicz, B.,
Johannsen, V. K., Joly, C. A., Jucker, T., Jung, I., Karminov, V., Kartawinata, K., Kearsley, E., Kenfack, D., Kennard, D. K., Kepfer-Rojas,
S., Keppel, G., Khan, M. L., Killeen, T. J., Kim, H. S., Kitayama, K., Köhl, M., Korjus, H., Kraxner, F., Kucher, D., Laarmann, D., Lang,
M., Lu, H., Lukina, N. V., Maitner, B. S., Malhi, Y., Marcon, E., Marimon, B. S., Marimon-Junior, B. H., Marshall, A. R., Martin, E. H.,
Meave, J. A., Melo-Cruz, O., Mendoza, C., Mendoza-Polo, I., Miscicki, S., Merow, C., Monteagudo Mendoza, A., Moreno, V. S., Mukul,
810 S. A., Mundhenk, P., Nava-Miranda, M. G., Neill, D., Neldner, V. J., Nevenic, R. V., Ngugi, M. R., Niklaus, P. A., Oleksyn, J., Ontikov,
P., Ortiz-Malavasi, E., Pan, Y., Paquette, A., Parada-Gutierrez, A., Parfenova, E. I., Park, M., Parren, M., Parthasarathy, N., Peri, P. L.,
Pfautsch, S., Picard, N., Piedade, M. T. F., Piotta, D., Pitman, N. C. A., Poulsen, A. D., Poulsen, J. R., Pretzsch, H., Ramirez Arevalo,
F., Restrepo-Correa, Z., Rodeghiero, M., Rolim, S. G., Roopsind, A., Rovero, F., Rutishauser, E., Saikia, P., Salas-Eljatib, C., Saner, P.,
Schall, P., Schelhaas, M.-J., Schepaschenko, D., Scherer-Lorenzen, M., Schmid, B., Schöngart, J., Searle, E. B., Seben, V., Serra-Diaz,
815 J. M., Sheil, D., Shvidenko, A. Z., Silva-Espejo, J. E., Silveira, M., Singh, J., Sist, P., Slik, F., Sonké, B., Souza, A. F., Stereńczak, K. J.,
Svenning, J.-C., Svoboda, M., Swanepoel, B., Targhetta, N., Tchebakova, N., ter Steege, H., Thomas, R., Tikhonova, E., Umunay, P. M.,
Usoltsev, V. A., Valencia, R., Valladares, F., van der Plas, F., Van Do, T., van Nuland, M. E., Vasquez, R. M., Verbeeck, H., Viana, H.,
Vibrans, A. C., Vieira, S., von Gadow, K., Wang, H.-F., Watson, J. V., Werner, G. D. A., Wisser, S. K., Wittmann, F., Woell, H., Wortel, V.,
Zagt, R., Zawila-Niedzwiecki, T., Zhang, C., Zhao, X., Zhou, M., Zhu, Z.-X., Zo-Bi, I. C., Gann, G. D., and Crowther, T. W.: Integrated
820 global assessment of the natural forest carbon potential, *Nature* 2023, pp. 1–10, <https://doi.org/10.1038/s41586-023-06723-z>, 2023.
- Oldenburg, D., Wills, R. C., Armour, K. C., and Thompson, L. A.: Resolution Dependence of Atmosphere–Ocean Interac-
tions and Water Mass Transformation in the North Atlantic, *Journal of Geophysical Research: Oceans*, 127, e2021JC018102,
<https://doi.org/10.1029/2021JC018102>, 2022.
- Papritz, L. and Grams, C. M.: Linking Low-Frequency Large-Scale Circulation Patterns to Cold Air Outbreak Formation in the Northeastern
825 North Atlantic, *Geophysical Research Letters*, 45, 2542–2553, <https://doi.org/10.1002/2017GL076921>, 2018.
- Papritz, L. and Spengler, T.: A Lagrangian Climatology of Wintertime Cold Air Outbreaks in the Irminger and Nordic Seas and Their Role
in Shaping Air–Sea Heat Fluxes, *Journal of Climate*, 30, 2717–2737, <https://doi.org/10.1175/JCLI-D-16-0605.1>, 2017.
- Papritz, L., Pfahl, S., Sodemann, H., and Wernli, H.: A Climatology of Cold Air Outbreaks and Their Impact on Air–Sea Heat Fluxes in the
High-Latitude South Pacific, *Journal of Climate*, 28, 342–364, <https://doi.org/10.1175/JCLI-D-14-00482.1>, 2015.
- 830 Parzen, E.: On Estimation of a Probability Density Function and Mode, <https://doi.org/10.1214/aoms/1177704472>, 33, 1065–1076,
<https://doi.org/10.1214/AOMS/1177704472>, 1962.
- Pellichero, V., Sallée, J.-B., Chapman, C. C., and Downes, S. M.: The southern ocean meridional overturning in the sea-ice sector is driven
by freshwater fluxes, *Nature Communications*, 9, 1789, <https://doi.org/10.1038/s41467-018-04101-2>, 2018.
- Pickart, R. S., Spall, M. A., Ribergaard, M. H., Moore, G. W., and Milliff, R. F.: Deep convection in the Irminger Sea forced by the Greenland
835 tip jet, *Nature* 2003 424:6945, 424, 152–156, <https://doi.org/10.1038/nature01729>, 2003.
- Portmann, R., Beyerle, U., Davin, E., Fischer, E. M., De Hertog, S., and Schemm, S.: Global forestation and deforestation affect remote
climate via adjusted atmosphere and ocean circulation, *Nature Communications* 2022 13:1, 13, 1–11, <https://doi.org/10.1038/s41467-022-33279-9>, 2022.
- Putrasahan, D. A., Lohmann, K., von Storch, J., Jungclaus, J. H., Gutjahr, O., and Haak, H.: Surface Flux Drivers for the Slowdown of
840 the Atlantic Meridional Overturning Circulation in a High-Resolution Global Coupled Climate Model, *Journal of Advances in Modeling
Earth Systems*, 11, 1349–1363, <https://doi.org/10.1029/2018MS001447>, 2019.

Rahmstorf, S.: Ocean circulation and climate during the past 120,000 years, *Nature*, 419, 207–214, <https://doi.org/10.1038/nature01090>, 2002.

845 Rahmstorf, S.: Is the Atlantic Overturning Circulation Approaching a Tipping Point?, *Oceanography*,
<https://doi.org/10.5670/OCEANOLOG.2024.501>, 2024.

Rahmstorf, S., Box, J. E., Feulner, G., Mann, M. E., Robinson, A., Rutherford, S., and Schaffernicht, E. J.: Exceptional twentieth-century slowdown in Atlantic Ocean overturning circulation, *Nature Climate Change*, 5, 475–480, <https://doi.org/10.1038/nclimate2554>, 2015.

850 Renfrew, I. A., Huang, J., Semper, S., Barrell, C., Terpstra, A., Pickart, R. S., Våge, K., Elvidge, A. D., Spengler, T., Strehl, A., and Weiss, A.: Coupled atmosphere–ocean observations of a cold-air outbreak and its impact on the Iceland Sea, *Quarterly Journal of the Royal Meteorological Society*, 149, 472–493, <https://doi.org/10.1002/qj.4418>, 2023.

Renssen, H., Goosse, H., and Fichefet, T.: On the non-linear response of the ocean thermohaline circulation to global deforestation, *Geophysical Research Letters*, 30, <https://doi.org/10.1029/2002GL016155>, 2003.

Rohatyn, S., Yakir, D., Rotenberg, E., and Carmel, Y.: Limited climate change mitigation potential through forestation of the vast dryland regions, *Science*, 377, 1436–1439, <https://doi.org/10.1126/science.abm9684>, 2022.

855 Schemm, S.: Regional Trends in Weather Systems Help Explain Antarctic Sea Ice Trends, *Geophysical Research Letters*, 45, 7165–7175, <https://doi.org/10.1029/2018GL079109>, 2018.

Schemm, S., Ciasto, L. M., Li, C., and Kvamstø, N. G.: Influence of Tropical Pacific Sea Surface Temperature on the Genesis of Gulf Stream Cyclones, *Journal of the Atmospheric Sciences*, 73, 4203–4214, <https://doi.org/10.1175/JAS-D-16-0072.1>, 2016.

860 Snyder, P. K.: The influence of tropical deforestation on the Northern Hemisphere climate by atmospheric teleconnections, *Earth Interactions*, 14, 1–34, <https://doi.org/10.1175/2010EI280.1>, 2010.

Snyder, P. K., Delire, C., and Foley, J. A.: Evaluating the influence of different vegetation biomes on the global climate, *Climate Dynamics*, 23, 279–302, <https://doi.org/10.1007/S00382-004-0430-0/TABLES/10>, 2004.

Sprenger, M. and Wernli, H.: The LAGRANTO Lagrangian analysis tool – version 2.0, *Geoscientific Model Development*, 8, 2569–2586, <https://doi.org/10.5194/gmd-8-2569-2015>, 2015.

865 Suckow, M. A., Weisbroth, S. H., and Franklin, C. L.: Chapter 4 - Density and pressure in the oceans, in: *Seawater (Second Edition)*, pp. 39–60, Butterworth-Heinemann, Oxford, second edition edn., ISBN 978-0-7506-3715-2, <https://doi.org/https://doi.org/10.1016/B978-075063715-2/50005-8>, 1995.

Sverdrup, H. U.: Wind-Driven Currents in a Baroclinic Ocean; with Application to the Equatorial Currents of the Eastern Pacific, *Proceedings of the National Academy of Sciences*, 33, 318–326, <https://doi.org/10.1073/pnas.33.11.318>, 1947.

870 Svingen, K., Brakstad, A., Våge, K., von Appen, W.-J., and Papritz, L.: The Impact of Cold-Air Outbreaks and Oceanic Lateral Fluxes on Dense-Water Formation in the Greenland Sea from a 10-Year Moored Record (1999–2009), *Journal of Physical Oceanography*, 53, 1499–1517, <https://doi.org/10.1175/JPO-D-22-0160.1>, 2023.

Swann, A. L. S., Fung, I. Y., and Chiang, J. C. H.: Mid-latitude afforestation shifts general circulation and tropical precipitation, *PNAS*, 109, <https://doi.org/10.1073/pnas.1116706108>, 2012.

875 van Westen, R. M. and Dijkstra, H. A.: Asymmetry of AMOC Hysteresis in a State-Of-The-Art Global Climate Model, *Geophysical Research Letters*, 50, e2023GL106 088, <https://doi.org/10.1029/2023GL106088>, 2023.

van Westen, R. M. and Dijkstra, H. A.: Persistent climate model biases in the Atlantic Ocean’s freshwater transport, *Ocean Science*, 20, 549–567, <https://doi.org/10.5194/OS-20-549-2024>, 2024.



- van Westen, R. M. v., Kliphuis, M., and Dijkstra, H. A.: Physics-based early warning signal shows that AMOC is on tipping course, *Science Advances*, 10, 1189, <https://doi.org/10.1126/SCIADV.ADK1189>, 2024.
- 880
- Wang, Y., Yan, X., and Wang, Z.: The biogeophysical effects of extreme afforestation in modeling future climate, *Theoretical and Applied Climatology*, 118, 511–521, <https://doi.org/10.1007/s00704-013-1085-8>, 2014.
- Weber, J., King, J. A., Abraham, N. L., Grosvenor, D. P., Smith, C. J., Shin, Y. M., Lawrence, P., Roe, S., Beerling, D. J., and Martin, M. V.: Chemistry-albedo feedbacks offset up to a third of forestation’s CO₂ removal benefits, *Science*, 383, 860–864, 885 <https://doi.org/10.1126/SCIENCE.ADG6196>, 2024.
- Winckler, J., Lejeune, Q., Reick, C. H., and Pongratz, J.: Nonlocal Effects Dominate the Global Mean Surface Temperature Response to the Biogeophysical Effects of Deforestation, *Geophysical Research Letters*, 46, 745–755, <https://doi.org/10.1029/2018GL080211>, 2019.
- Windisch, M. G., Davin, E. L., and Seneviratne, S. I.: Prioritizing forestation based on biogeochemical and local biogeophysical impacts, *Nature Climate Change*, <https://doi.org/10.1038/s41558-021-01161-z>, 2021.
- 890 Wunsch, C. and Roemmich, D.: Is the North Atlantic in Sverdrup Balance?, *Journal of Physical Oceanography*, 15, 1876–1880, [https://doi.org/10.1175/1520-0485\(1985\)015<1876:ITNAIS>2.0.CO;2](https://doi.org/10.1175/1520-0485(1985)015<1876:ITNAIS>2.0.CO;2), 1985.
- Yeager, S.: Topographic Coupling of the Atlantic Overturning and Gyre Circulations, *Journal of Physical Oceanography*, 45, 1258–1284, <https://doi.org/10.1175/JPO-D-14-0100.1>, 2015.
- Zhang, R. and Vallis, G. K.: The Role of Bottom Vortex Stretching on the Path of the North Atlantic Western Boundary Current and on the 895 Northern Recirculation Gyre, *Journal of Physical Oceanography*, 37, 2053–2080, <https://doi.org/10.1175/JPO3102.1>, 2007.